

Suppression of Mainbeam Deceptive Jammer with FDA-MIMO Radar

Lan, Lan; Xu, Jingwei; Liao, Guisheng; Zhang, Yuhong ; Fioranelli, Francesco; Cheung So, Hing

DOI

[10.1109/TVT.2020.3014689](https://doi.org/10.1109/TVT.2020.3014689)

Publication date

2020

Document Version

Final published version

Published in

IEEE Transactions on Vehicular Technology

Citation (APA)

Lan, L., Xu, J., Liao, G., Zhang, Y., Fioranelli, F., & Cheung So, H. (2020). Suppression of Mainbeam Deceptive Jammer with FDA-MIMO Radar. *IEEE Transactions on Vehicular Technology*, 69(10), 11584-11598. [9161264]. <https://doi.org/10.1109/TVT.2020.3014689>

Important note

To cite this publication, please use the final published version (if applicable). Please check the document version above.

Copyright

Other than for strictly personal use, it is not permitted to download, forward or distribute the text or part of it, without the consent of the author(s) and/or copyright holder(s), unless the work is under an open content license such as Creative Commons.

Takedown policy

Please contact us and provide details if you believe this document breaches copyrights. We will remove access to the work immediately and investigate your claim.






Green Open Access added to TU Delft Institutional Repository

'You share, we take care!' - Taverne project

<https://www.openaccess.nl/en/you-share-we-take-care>

Otherwise as indicated in the copyright section: the publisher is the copyright holder of this work and the author uses the Dutch legislation to make this work public.

Suppression of Mainbeam Deceptive Jammer With FDA-MIMO Radar

Lan Lan , Member, IEEE, Jingwei Xu , Member, IEEE, Guisheng Liao, Senior Member, IEEE, Yuhong Zhang , Senior Member, IEEE, Francesco Fioranelli , Senior Member, IEEE, and Hing Cheung So , Fellow, IEEE

Abstract—Suppression of radar-to-radar jammers, especially the mainbeam jammers, has been an urgent demand in vehicular sensing systems with the expected increased number of vehicles equipped with radar systems. This paper deals with the suppression of mainbeam deceptive jammers with frequency diverse array (FDA)-multiple-input multiple-output (MIMO) radar, utilizing its extra degrees-of-freedom (DOFs) in the range domain. At the modelling stage, false targets, which lag several pulses behind the true target, are considered as a typical form of mainbeam jammers. To this end the data-independent beamforming is performed to suppress false targets by nulling at the equivalent transmit beam-pattern with an appropriate frequency increment. However, the suppression performance degrades in the presence of transmit spatial frequency mismatch, which could be induced by quantization errors, angle estimation errors and frequency increment errors. To solve this problem, a preset broadened nulling beamformer (PBN-BF) is proposed by placing artificial interferences with appropriate powers around the nulls of the equivalent transmit beam-pattern. In such a way, effective suppression of deceptive jammer can be guaranteed owing to the broadened notches. At the analysis stage, numerical results in a scenario with multiple unmanned aerial vehicles (UAVs) are provided to illustrate the effectiveness of the devised data-independent BF, and the signal-to-interference-plus-noise ratio is improved compared with the conventional data-independent BF.

Index Terms—Mainbeam deceptive jammer suppression, FDA-MIMO radar, unmanned aerial vehicles (UAVs), data-independent beamforming, joint transmit-receive spatial frequency, artificial interference.

I. INTRODUCTION

ARRAY signal processing has been widely used in civilian applications, including autonomous vehicles (AVs),

Manuscript received March 25, 2020; revised June 2, 2020 and July 28, 2020; accepted August 3, 2020. Date of publication August 6, 2020; date of current version October 22, 2020. This work was supported in part by the National Nature Science Foundation of China under Grants 61931016 and 61911530246, and in part by the Young Talent Fund of University Association for Science and Technology in Shaanxi Province under Grant 20180103. The review of this article was coordinated by Prof. Wan Choi. (Corresponding authors: Lan Lan; Guisheng Liao.)

Lan Lan, Jingwei Xu, and Guisheng Liao are with the National Key Laboratory of Radar Signal Processing, Xidian University, Xi'an 710071, China (e-mail: lanlan_xidian@foxmail.com; xujingwei1987@163.com; liaogs@xidian.edu.cn).

Yuhong Zhang is with the School of Electronic Engineering, Xidian University, Xi'an 710071, China (e-mail: yuhzhang@xidian.edu.cn).

Francesco Fioranelli is with the Department of Microelectronics, TU Delft, 2628CD, Netherlands (e-mail: F.Fioranelli@tudelft.nl).

Hing Cheung So is with the Department of Electronic Engineering, City University of Hong Kong, Kowloon, Hong Kong (e-mail: hcso@ee.cityu.edu.hk).

Digital Object Identifier 10.1109/TVT.2020.3014689

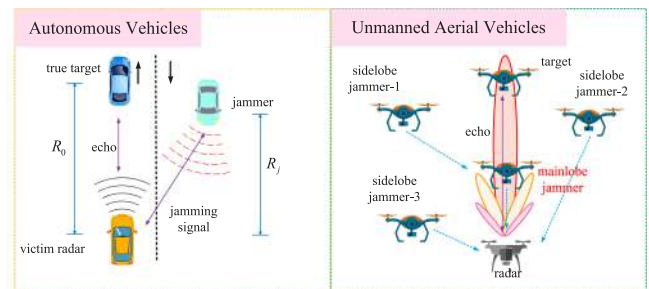


Fig. 1. Pictorial sketch of relevant jamming scenarios for ground and aerial vehicles applications.

unmanned aerial vehicles (UAVs), as well as traffic control [1]–[4]. For vehicular sensing systems, radar techniques has obtained increasing attention due to its all-day and all-weather operational ability for detecting range and radial velocity [5], [6]. However, increasing number of vehicles with multiple radar on-board, anti-jamming capabilities become an urgent demand as there are some intended and unintended jammers from surroundings (See Fig. 1) [7]. Those jammers degrade the detection capabilities and can cause sensor blindness, which in turn impacts the autonomy and safety of the system [8]. Among various types of jammers, the deceptive jammer, which can intercept radar signals and generate false targets based on an appropriate time modulation in digital radio frequency memory (DRFM) [9], poses a significant threat to existing radar systems. It makes detecting the target a rather difficult task when false targets are located within the mainbeam.

In these circumstances, various methods to mitigate deceptive jammers have been investigated. Generally, signals corresponding to different radars must be separable at least in one dimension, such as time, frequency, space, or code/waveform [10]. In this respect, signal processing techniques including antenna polarization, separating time slots/radio channels, antenna nulling and coding approaches have been proposed in automotive vehicles, which were summarized in [11]. For mainbeam deceptive jammers, traditional approaches have been proposed to discriminate the true and false targets in various domains, such as time [12], frequency [13], as well as polarization [14]. However, emulated false targets from the mainbeam cannot be easily discriminated and suppressed with traditional techniques. Hence, there is an urgent demand for anti-jammer capabilities in emerging radar systems.

Recently, the frequency diverse array (FDA) radar, which provides an advantage of increased degrees-of-freedom (DOFs) in the range domain, has been widely investigated [15]–[17]. Different from the phased array radar which provides only angle-dependent transmit beampattern, a range-angle-time-dependent beampattern can be generated in FDA by introducing a small frequency increment across adjacent array elements [18]. Much attention has been paid on the analyses of the transmit beampattern [19]–[21]. However, in standard FDA, frequencies of elements are increased linearly, which yields a coupled ‘S’-shape beampattern in the joint angle-range domain, leading to possible ambiguities in the range-angle dimension during the target localization process. Furthermore, the time-variant beampattern is not desired for target localization in practice. To cope with these problems, the multiple-input multiple-output (MIMO) technique is combined with the FDA framework. In FDA-MIMO radar, the transmit waveforms are separated in the receiver, and the time-independent transmit steering vector is obtained. It has been found that the FDA-MIMO radar is capable of fulfilling practical tasks that the conventional MIMO radar cannot handle [22]–[24].

Compared with the conventional MIMO radar whose transceive beampattern is only angle-dependent, mainbeam deceptive jammer can not be effectively suppressed due to lack of controllable DOFs. In contrast, extra DOFs in the range domain is obtained with FDA-MIMO radar whose transceive beampattern is range-angle-dependent. As pseudo-randomly distributed false targets are generated, they have different transmit steering vectors. In this respect, the true and false targets with an identical angle are distinguishable in the range domain. Several approaches have been considered to suppress the mainbeam deceptive jamming with FDA-MIMO radar [25]–[27]. It is noteworthy that the signal model in [25] is a special case due to missing the time delay term. Besides, it is not feasible to find perfectly orthogonal waveforms for all Doppler and delay pairs in practice. The signal model has been re-derived in [26], [27], where the estimation of jammer-plus-noise covariance matrix was addressed in [26], and the ability of jammer suppression was studied under the condition of *a priori* knowledge in [27]. However, the aforementioned methods are developed based on data-dependent beamforming, where the training data was used to estimate the jammer-plus-noise covariance matrix. Furthermore, this is still a difficult task for sample selection, because training samples collected from adjacent range bins are no longer independent and identically distributed. As a result, it is worth an investigation of mainbeam deceptive jammer suppression with data-independent beamforming. Furthermore, suppression performance degrades in the presence of mismatches, such as range quantization errors and angle estimation errors, which have not been considered in the existing literature.

This discussion motivates the present study which addresses mainbeam deceptive jammer suppression using data-independent beamforming with FDA-MIMO radar. At the modelling stage, false targets, which lag several pulses behind the true target, are considered. Selecting a proper frequency increment and performing data-independent beamforming,

false targets which dwell at nulls of the equivalent transmit beampattern are suppressed. Specifically, only the false target generated after delay larger than one pulse repetition time (PRT), can be suppressed. Furthermore, considering the presence of transmit spatial frequency mismatch, which may be caused by quantization errors, angle estimation errors and frequency increment errors, a preset broadened nulling beamformer (PBN-BF) is developed to guarantee effective suppression. In this context, artificial interferences with appropriate powers are imposed to broaden the nulls, and the covariance matrix is constructed with artificial interferences. At the analysis stage, we consider the scenario of multiple UAVs, where other UAVs can generate intentional deceptive or accidental jamming. It is worth noticing that, the detection range of some UAVs with large models can operate at hundreds of kilometers [28]–[30]. The suppression performance in UAVs is evaluated by the output power of data-independent 2-D BF as well as the output signal-to-interference-plus-noise ratio (SINR). Numerical results validate the effectiveness of the suppression of mainbeam deceptive jammer.

The remainder of this paper is organized as follows. Section II presents the signal model and the principle of the mainbeam deceptive jammer suppression with FDA-MIMO radar. To enhance the robustness of jammer suppression in the presence of transmit spatial frequency mismatch, the PBN-BF method is investigated in Section III. Simulation results are given in Section IV. Conclusions are drawn in Section V.

Notations: Boldface is used for vectors \mathbf{x} (lower case), whose n -th entry is $x(n)$, and matrices \mathbf{A} (upper case), whose entry in the m -th row and the n -th column is $[\mathbf{A}]_{m,n}$. The transpose, the conjugate, and the conjugate transpose operators are denoted by the symbols $(\cdot)^T$, $(\cdot)^*$, and $(\cdot)^H$, respectively. $\text{diag}(\cdot)$ indicates the diagonal matrix. \mathbf{I}_N and $\mathbf{1}_N$ denote respectively the $N \times N$ identity matrix and the $N \times 1$ vector with all elements being one. \mathbb{C}^N , \mathbb{R}^N , and \mathbb{N}^+ are respectively the sets of N -dimensional vectors of complex numbers, N -dimensional vectors of real numbers and positive integers. For any $\mathbf{x} \in \mathbb{C}^N$, $\|\mathbf{x}\|_2$ denotes its Euclidian norm. \odot and \otimes represent the Hadamard product and the Kronecker product, respectively. The letter j represents the imaginary unit (i.e. $j = \sqrt{-1}$). For any complex number z , $|z|$ is used to denote the modulus of z . Finally, $[a, b]$ indicates a closed interval of \mathbb{R} with a and b being the beginning and the end, respectively.

II. DECEPTIVE JAMMER SUPPRESSION WITH FDA-MIMO RADAR

A. Signal Model of FDA-MIMO Radar

Consider a colocated MIMO radar with M omnidirectional transmit and receive elements in a uniform linear array. The frequency increment Δf is introduced in the transmit array with the first element being the reference. Thus, the carrier frequency of the m -th element is

$$f_m = f_0 + (m - 1)\Delta f, \quad m = 1, 2, \dots, M, \quad (1)$$

where f_0 is the reference carrier frequency. Assume that a phase-coded pulse, composed of P subpulses, is transmitted by each

element, and the transmitted signal of the m -th element is

$$s_m(t) = \sqrt{\frac{E}{M}} x_m(t) u\left(\frac{t}{T_p}\right) e^{j2\pi f_m t}, \quad (2)$$

where $u(t) = \begin{cases} 1, & 0 \leq t \leq 1 \\ 0, & \text{else} \end{cases}$, E is the transmitted energy, T_p is the radar pulse duration, and $x_m(t)$ the m -th complex envelope signal given by

$$x_m(t) = \frac{1}{\sqrt{\tau_b}} \sum_{l=1}^P \varphi_m(l) u\left[\frac{t - (l-1)\tau_b}{\tau_b}\right], \quad l = 1, \dots, P, \quad (3)$$

where τ_b is the length of each subpulse with $\tau_b = \frac{T_p}{P}$ and

$$\varphi_m(l) = e^{j\phi_m(l)}, \quad (4)$$

where $\phi_m(l) \in [0, 2\pi]$.

Suppose a target in far-field at angle θ_0 and range R_0 , the signal received by the n -th ($n = 1, 2, \dots, M$) element is written as

$$\begin{aligned} y_n(t) &= \beta \sum_{m=1}^M x_m(t - \tau_0) e^{j2\pi f_m(t - \tau_{m,n})} \\ &\approx \beta e^{j2\pi f_0(t - \tau_0)} e^{j2\pi \frac{d}{\lambda_0}(n-1)\sin(\theta_0)} \\ &\quad \sum_{m=1}^M x_m(t - \tau_0) e^{j2\pi \Delta f(m-1)(t - \tau_0)} e^{j2\pi \frac{d}{\lambda_0}(m-1)\sin(\theta_0)}, \end{aligned} \quad (5)$$

where $x_m(t)$ is the complex envelope of the m -th transmitted signal, $\tau_{m,n} = \frac{2R_0 - d(n-1)\sin(\theta_0) - d(m-1)\sin(\theta_0)}{c}$ denotes the round-trip propagation delay from the m -th transmit element to the n -th receive element, $\tau_0 = \frac{2R_0}{c}$, c is the speed of light, β is the complex echo amplitude (accounting for the transmit amplitude, phase, target reflectivity, and channels propagation effects), d is the inter-element spacing, and λ_0 is the wavelength. The approximation holds true as long as $(M-1)^2 \Delta f \frac{d}{c} \ll 1$. Notice that as the method investigates beamforming in the spatial dimension and this is independent of Doppler processing, the Doppler term is neglected in the analysis for the sake of simplicity.

After matched filtering with M waveforms, by stacking the received signals into an $M^2 \times 1$ space-time snapshot, we express the received signal of the target in a simple form as

$$\mathbf{y}_s = \alpha_0 \mathbf{r} \odot [\mathbf{b}(\theta_0) \otimes \mathbf{a}(R_0, \theta_0)], \quad (6)$$

where $\alpha_0 = \beta e^{-j2\pi f_0 \tau_0}$, $\mathbf{r} \in \mathbb{C}^{M^2}$ indicates the output vector of the matched filtering, $\mathbf{a}(R_0, \theta_0) \in \mathbb{C}^M$ and $\mathbf{b}(\theta_0) \in \mathbb{C}^M$ represent the transmit and receive steering vectors, respectively, which have the forms of

$$\begin{aligned} \mathbf{a}(R_0, \theta_0) &= \left[1, e^{j2\pi \frac{d}{\lambda_0} \sin(\theta_0)} e^{-j2\pi \Delta f \frac{2R_0}{c}}, \dots, \right. \\ &\quad \left. e^{j2\pi \frac{d}{\lambda_0} (M-1) \sin(\theta_0)} e^{-j2\pi \Delta f (M-1) \frac{2R_0}{c}} \right]^T, \end{aligned} \quad (7a)$$

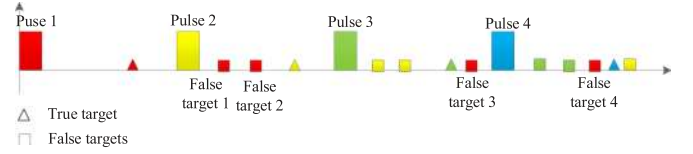


Fig. 2. Generation of false targets.

$$\mathbf{b}(\theta_0) = \left[1, e^{j2\pi \frac{d}{\lambda_0} \sin(\theta_0)}, \dots, e^{j2\pi \frac{d}{\lambda_0} (M-1) \sin(\theta_0)} \right]^T. \quad (7b)$$

Please refer to Appendix A for detailed derivations.

Consider a false target generator (FTG) locating at angle θ_j and range R_j which also acts as a target for the victim radar. In this case, the angle of the mainbeam deceptive jammer is the same as that of the true target, i.e., $\theta_j = \theta_0$, and the distance from the target and the distance from the interferer are identical, i.e., $R_j = R_0$. The FTG intercepts the radar waveforms and generates Q pseudo-randomly distributed false targets to deceive the victim radar. Hence, the actual range of the false target is larger than that of the true target, and two different kinds of false targets generation strategies are considered. The former can repeat false targets very fast, and they are settled in the same receive pulse with the true target. The latter can generate false targets with relatively large time delays, hence, they lag at least one pulse behind the true target. We focus on the latter in this paper. Fig. 2 shows the generation of false targets, where different colors represent different slow time pulses, i.e., range ambiguity regions. Assume that the true target is unambiguous. The “false targets 1 and 2” have one delayed pulse (i.e., the range ambiguity index is 1) while it is two for the “false target 3” and three for the “false target 4,” respectively. As is intuitively shown, the true and false targets are distinguishable due to the difference of delayed pulses.

It is worth emphasizing that, the steering vectors for all false targets, generated by an identical FTG, are assumed the same in [25], which is a simplified case. In contrast, from a more practical point of view, different false targets have different steering vectors due to time delay in FTG. Take the q -th ($q = 1, 2, \dots, Q$) false target for example, its actual range is calculated as $R_q = R_j + \frac{c\Delta t_q}{2}$ with Δt_q being the time delay in FTG. Similarly, after matched filtering, the received signal of the q -th false target takes the form

$$\mathbf{y}_q = \alpha_q \mathbf{r} \odot [\mathbf{b}(\theta_0) \otimes \mathbf{a}(R_q, \theta_0)], \quad (8)$$

where α_q is the complex amplitude of the q -th false target. Besides, the velocities of the true target and deceptive jammers are the same, thus, the effect of Doppler on the beamforming for moving targets can be ignored.

Considering all received signals in an identical pulse, we have

$$\mathbf{y} = \mathbf{y}_s + \sum_{q=1}^Q \mathbf{y}_q + \mathbf{n}, \quad (9)$$

where $\mathbf{n} \in \mathbb{C}^{M^2}$ indicates the noise vector.

B. Mainbeam Deceptive Jammer Suppression With Data-Independent Beamforming

Data-independent beamforming is performed for deceptive jammer suppression in this subsection. It is worth noting that two assumptions are considered, i.e., (i) *a priori* coarse knowledge of the true target, i.e., the number of delayed pulses, is available; (ii) the number of delayed pulses for the true target and false ones are different, since the false targets are time delayed. Specifically, the method can only deal with the case that the delays of the false targets are larger than one PRT. According to the transmit and receive steering vectors, the transmit spatial frequencies of the true target and the q -th false target in FDA-MIMO radar are respectively defined as

$$f_T^s = -\Delta f \frac{2R_0}{c} + \frac{d}{\lambda_0} \sin(\theta_0), \quad (10a)$$

$$f_T^q = -\Delta f \frac{2R_q}{c} + \frac{d}{\lambda_0} \sin(\theta_0). \quad (10b)$$

Furthermore, it follows from the receive steering vector in (7) that the receive spatial frequencies are $f_R^s = f_R^q = \frac{d}{\lambda_0} \sin(\theta_0)$.

As stated in (10), the transmit spatial frequency is range-dependent, and the range-dependence compensation can be implemented henceforward by applying a compensating vector range-by-range on the received data [31], namely

$$\mathbf{h}(\tilde{r}) = \left[1, e^{j2\pi\Delta f \frac{2\tilde{r}}{c}}, \dots, e^{j2\pi\Delta f (M-1) \frac{2\tilde{r}}{c}} \right]^T, \quad (11)$$

where \tilde{r} is obtained with the range bin number and bin size. Furthermore, the compensating vector in the joint transmit-receive spatial frequency domain is given by

$$\mathbf{g} = \mathbf{1}_M \otimes \mathbf{h}(\tilde{r}). \quad (12)$$

Then, the compensation procedure is performed as $\hat{\mathbf{y}} = \mathbf{y} \odot \mathbf{g}$. Suppose that the numbers of delayed pulses for the true target and the q -th false target are p_s and p_f ($p_f > p_s$), respectively. After compensation, denoting by r_Δ the the principal range difference, the remaining range values of the true and the q -th false target are $R_0 - \tilde{r} = r_\Delta + p_s R_u$ and $R_q - \tilde{r} = r_\Delta + p_f R_u$, respectively, where $R_u = \frac{c}{2f_r}$ denotes the maximum unambiguous range with f_r being the pulse repetition frequency (PRF). For simplicity, assume that $r_\Delta = 0$, thus, the transmit spatial frequencies corresponding to the true target and the q -th false target are expressed as

$$\tilde{f}_T^s = -\frac{2\Delta f}{c} p_s R_u + \frac{d}{\lambda_0} \sin(\theta_0), \quad (13a)$$

$$\tilde{f}_T^q = -\frac{2\Delta f}{c} p_f R_u + \frac{d}{\lambda_0} \sin(\theta_0). \quad (13b)$$

Subtracting (13a) from (13b), we have the difference between the transmit spatial frequencies

$$f_T^\Delta = \tilde{f}_T^s - \tilde{f}_T^q = p \frac{2\Delta f}{c} R_u = p \frac{\Delta f}{f_r} = p(z + u), \quad (14)$$

where $z = \text{int}(\Delta f / f_r)$ is the integer part, $p = p_f - p_s$, $p > 1$ is the difference of delayed pulses between the true and false

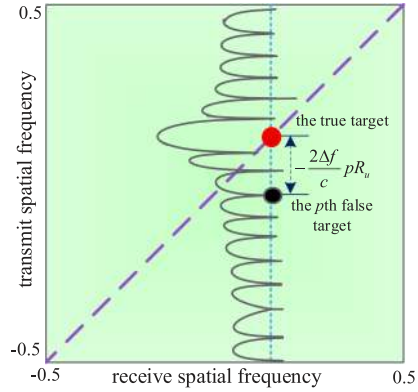


Fig. 3. Positions of true and false targets in joint transmit-receive domain.

targets. The frequency increment is expressed as

$$\Delta f = (z + u) f_r. \quad (15)$$

Due to 2π periodicity of the phase difference, the influence of z can be ignored. In order to guarantee effective discrimination between the true and false targets, $f_T^\Delta \notin \mathbb{Z}^+$ must be satisfied, which leads to $pu \notin \mathbb{Z}^+$. If $pu \in \mathbb{Z}^+$, false target suppression becomes invalid because the transmit frequencies of the true target and the false target are identical. For simplicity, assume henceforth that $p_s = 0$, thus, the equivalent normalized transmit beampattern in the transmit spatial domain is expressed as

$$P(f_T) = \frac{1}{M} \cdot \frac{\sin(\pi M f_T)}{\sin(\pi f_T)} e^{j2\pi(M-1)f_T}. \quad (16)$$

where $f_T = \frac{d}{\lambda_0} \sin(\theta)$. Please refer to Appendix B for detailed derivations. The nulls of the pattern occur when the numerator of $P(f_T)$ is zero and the denominator is non-zero, that is, $M\pi f_T = k\pi$, $k \in \mathbb{Z}^+$ and $\pi f_T \neq k\pi$, $k \in \mathbb{Z}^+$ respectively. This results in

$$f_T = \frac{k}{M}. \quad (17)$$

For the first null with frequency $f_T = \frac{1}{M}$, if $u = \frac{1}{M}$, the false target which is delayed by one pulse is exactly settled at the first null. Thus, the frequency increment in (15) becomes:

$$\Delta f = f_r \left(z + \frac{1}{M} \right). \quad (18)$$

Moreover, for the false target with p delayed pulses compared with that of the true target, the frequency increment is assigned as

$$\Delta f = f_r \left(z + \frac{i}{p_f M} \right), \quad i = 1, 2, \dots, M-1. \quad (19)$$

Hence, by substituting the designed frequency increment into (13b), the transmit spatial frequency of false target with p delayed pulses is equal to that of the p -th null, indicating that the false targets with 1 to $(M-1)$ delayed pulses can be suppressed because they correspond to the first to $(M-1)$ -th nulls of the beampattern. Fig. 3 shows the locations of true and false targets in the joint transmit-receive spatial frequency domain. It can be seen that the true target is located on a diagonal line because the transmit and receive spatial frequencies are identical, while the

false target with p delayed pulses is positioned exactly at the null of the equivalent transmit beampattern. It is due to the fact that p delayed pulses leads to an offset by $-\frac{2\Delta f}{c}pR_u$ in the transmit spatial frequency.

Then, received signals are processed through a transmit-receive 2-D BF, where the weight vector is written as

$$\mathbf{w}_C = \mathbf{u}(R_0, \theta_0) = \mathbf{b}(\theta_0) \otimes \tilde{\mathbf{a}}(\theta_0), \quad (20)$$

where $\tilde{\mathbf{a}}(\theta_0) = [1, e^{j2\pi\frac{d}{\lambda_0}\sin(\theta_0)}, \dots, e^{j2\pi\frac{d}{\lambda_0}(M-1)\sin(\theta_0)}]^T$ denotes the steering vector of the target after range compensation. For simplicity, $\tilde{\mathbf{a}}(\theta_0)$ is written as \mathbf{a}_0 in the rest of the paper.

III. SUPPRESSION IN THE PRESENCE OF TRANSMIT SPATIAL FREQUENCY MISMATCH

A. Motivation and Problem Formulation

In practice, false targets may not be exactly located at the presumed directions, which leads to a small deviation from their presumed nulls in the equivalent transmit beampattern. Hence, the performance of the deceptive jammer suppression with data-independent beamforming degrades. Such mismatch could be induced by quantization errors in the range and angle measurements. In this respect, the actual transmit spatial frequency of the q -th false target in the q -th null region is expressed as

$$\hat{f}_T^q = -\frac{2(\Delta f + \Delta f_\Delta)}{c}(pR_u + r_\Delta) + \frac{d}{\lambda_0}\sin(\theta_0 + \Delta\theta). \quad (21)$$

where $r_\Delta \neq 0$ indicates the presence of the quantization error [31], $\Delta\theta$ denotes the angle shift representing the DOA mismatch, and Δf_Δ denotes the frequency increment error.

Besides, the mismatch frequency is expressed as

$$f_\Delta = -D_{\Delta f}\frac{2pR_u}{c} - \Delta f\frac{2D_r}{c} + d\frac{\sin(D_\theta)}{\lambda_0}. \quad (22)$$

To address this problem, it is desired to broaden the beampattern notches in order to mitigate possible angle/quantization/frequency mismatches. Thus, the problem is formulated as

$$\begin{aligned} & \min_{\mathbf{w}_d} \max Z(\|\mathbf{w}_d^H \mathbf{a}(f_q)\|_2 - \xi) \\ & \text{subject to } \begin{cases} \mathbf{w}_d^H \mathbf{a}(\tilde{f}_T^s) = 1 \\ |f_q - \tilde{f}_T^q| \leq \Delta f_T, \forall f_q \in \Theta_q \end{cases}, \end{aligned} \quad (23)$$

where the function $Z(x) \triangleq \max\{x, 0\}$, $\mathbf{w}_d \in \mathbb{C}^{M^2}$ denotes the designed weight vector, f_q is an arbitrary transmit spatial frequency corresponding to the q -th null region, i.e., Θ_q , $\mathbf{a}(\tilde{f}_T^s) = [1, e^{j2\pi\tilde{f}_T^s}, \dots, e^{j2\pi(M-1)\tilde{f}_T^s}]^T \in \mathbb{C}^M$ denotes the target steering vector after range compensation, $\mathbf{a}(f_q) = [1, e^{j2\pi f_q}, \dots, e^{j2\pi(M-1)f_q}]^T \in \mathbb{C}^M$ denotes an arbitrary steering vector corresponding to the q -th null region, ξ is the predefined null depth, and Δf_T is the maximum permissible deviation which is relative to the mismatch.

B. PBN-BF for Mainbeam Deceptive Jammer Suppression

It is not easy to address the optimization (21) directly due to the large computational complexity. To this end we resort to a non-adaptive method by broadening the nulls of the beampattern to mitigate possible angle/quantization/frequency mismatches. Hence, the PBN-BF algorithm is designed by imposing artificial interferences with appropriate powers around the nulls of the false targets. More specifically, the PBN-BF method is elaborated as follows: (i) The jammer-plus-noise covariance matrix is constructed with artificial interferences instead of real data. (ii) The artificial interferences are uncorrelated, while the false targets generated by an identical FTG are correlated. This is feasible because the range and angle information of target is available while the information of false targets can be predicted. (iii) As the response of an array to interference depends on its strength [32], the powers of the artificial interferences are calculated in closed-forms according to a predefined depth of the desired null. (iv) In practice, the exact information about jammers is unknown. Hence, all possible notches should be broadened to adequately suppress false targets.

In the first stage, we calculate the initial jammer-plus-noise covariance matrix by imposing artificial interferences successively

$$\mathbf{R}_1 = \mathbf{R}_0 + \sigma_1^2 \mathbf{a}_1 \mathbf{a}_1^H, \quad (24)$$

where $\mathbf{a}_1 \in \mathbb{C}^M$ denotes the steering vector of the first artificial interference, $\mathbf{R}^{(0)} = \sigma_w^2 \mathbf{I}_{M^2} \in \mathbb{C}^{M \times M}$ with σ_w^2 being the noise power, σ_1^2 is the power of the first interference as

$$\sigma_1^2 = \frac{\sigma_w^2}{M} \cdot \frac{\beta_{01} - \xi}{\xi(1 - |\beta_{01}|^2)}, \quad (25)$$

where $\beta_{01} = \frac{\mathbf{a}_0^H \mathbf{a}_1}{M}$, and σ_w^2 is the variance of the Gaussian white noise.

When imposing the Q -th artificial interference signal, the final jammer-plus-noise covariance matrix with successive artificial interference construction is updated as

$$\mathbf{R}_Q = \mathbf{R}_0 + \sum_{q=1}^Q \sigma_q^2 \mathbf{a}_q \mathbf{a}_q^H, \quad (26)$$

where the power of the q -th interference is calculated as

$$\sigma_q^2 = \frac{\mathbf{a}_0^H (\mathbf{R}_{q-1})^{-1} (\mathbf{a}_q - \xi \mathbf{a}_0)}{\xi \mathbf{a}_0^H (\mathbf{R}_{q-1})^{-1} [\mathbf{a}_0 \mathbf{a}_q^H (\mathbf{R}_{q-1})^{-1} \mathbf{a}_q - \mathbf{a}_q \mathbf{a}_q^H (\mathbf{R}_{q-1})^{-1} \mathbf{a}_0]}. \quad (27)$$

Please refer to Appendix C for detailed derivations. Thus, the jammer-plus-noise covariance matrix is obtained as $\mathbf{R}_{j+n} = \mathbf{R}_Q$. The weight vector is calculated according to the minimum variance distortionless response (MVDR) BF as $\mathbf{w} = \frac{\mathbf{R}_{j+n}^{-1} \mathbf{a}_0}{[\mathbf{a}_0^H \mathbf{R}_{j+n}^{-1} \mathbf{a}_0]^{-1}}$.

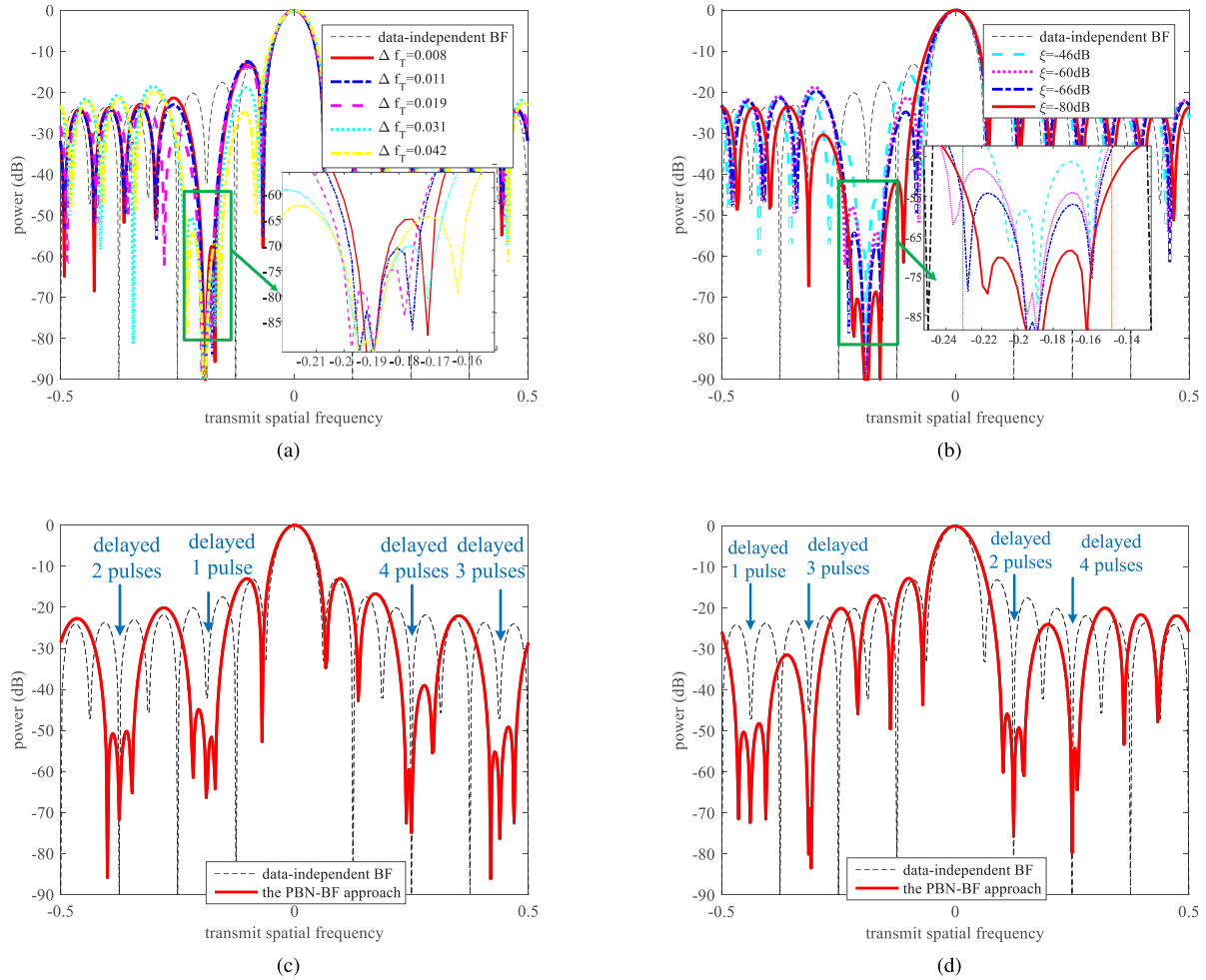


Fig. 4. Beam patterns with PBN-BF method. (a) Beam pattern with different Δf_T . (b) Beam pattern with different ξ . (c) Beam pattern with the first 4 broadened notches when $u = \frac{3}{M}$. (d) Beam pattern with the first 4 broadened notches when $u = \frac{7}{M}$.

However, it requires Q times to compute the jammer-plus-noise covariance when successively imposing artificial interferences. In order to reduce the computational complexity, another approach is proposed via concurrent artificial interference construction. The jammer-plus-noise covariance matrix is constructed as

$$\mathbf{R}_{j+n} = \sigma_w^2 \mathbf{I}_M + \mathbf{A} \mathbf{S}_j \mathbf{A}^H, \quad (28)$$

where $\mathbf{A} = [\mathbf{a}_1, \mathbf{a}_2, \dots, \mathbf{a}_Q] \in \mathbb{C}^{M \times Q}$, $\mathbf{S}_j = \text{diag}\{\sigma_1^2, \sigma_2^2, \dots, \sigma_Q^2\} \in \mathbb{C}^{Q \times Q}$ denotes the power matrix of the interference. The jammer-to-noise ratio (JNR) matrix is defined as

$$\begin{aligned} \Sigma_j &\triangleq \frac{\mathbf{S}_j}{\sigma_w^2} = \text{diag} \left\{ \frac{\sigma_1^2}{\sigma_w^2}, \frac{\sigma_2^2}{\sigma_w^2}, \dots, \frac{\sigma_Q^2}{\sigma_w^2} \right\} \\ &= \text{diag} \{ \rho_1, \rho_2, \dots, \rho_Q \}. \end{aligned} \quad (29)$$

Then, the inverse of the jammer-plus-noise covariance matrix is

$$\mathbf{R}_{j+n}^{-1} = \frac{1}{\sigma_w^2} \left[\mathbf{I}_M - \mathbf{A} (\mathbf{I}_Q + \Sigma_j \mathbf{A}^H \mathbf{A})^{-1} \Sigma_j \mathbf{A}^H \right]. \quad (30)$$

The weight vector \mathbf{w} is calculated as $\mathbf{w} = \Lambda \mathbf{R}_{j+n}^{-1} \mathbf{a}_0$ where the normalized coefficient Λ is given by

$$\Lambda = \left\{ \frac{M}{\sigma_w^2} \left[1 - \beta_{0J}^H (\mathbf{I}_Q + \Sigma_j \mathbf{A}^H \mathbf{A})^{-1} \Sigma_j M \beta_{0J} \right] \right\}^{-1}, \quad (31)$$

where $\beta_{0J} \triangleq \frac{\mathbf{A}^H \mathbf{a}_0}{M} \in \mathbb{C}^Q$ denotes the spatial correlation vector. Subsequently, the weight vector is obtained as

$$\mathbf{w} = \frac{\Lambda}{\sigma_w^2} \left[\mathbf{I}_M - \mathbf{A} (\mathbf{I}_Q + \Sigma_j \mathbf{A}^H \mathbf{A})^{-1} \Sigma_j \mathbf{A}^H \right] \mathbf{a}_0. \quad (32)$$

With a predefined depth at \mathbf{a}_q , the equivalent transmit beam pattern of the FDA-MIMO radar can be calculated as $P_{\text{opt}}(\mathbf{a}_q | \mathbf{a}_0) = \Lambda \mathbf{w}^H \mathbf{a}_q = \xi$. Solving the problem, the power of the q -th interference signal is expressed as

$$\sigma_q^2 = \frac{[\mathbf{h}^H \mathbf{P}^{-1}]_q}{[\beta_{0J}^H - \mathbf{h}^H \mathbf{P}^{-1} \mathbf{A}^H \mathbf{A}]_q} \sigma_w^2, \quad (33)$$

where $\mathbf{P} \in \mathbb{C}^{Q \times Q}$ with $[\mathbf{P}]_{i,j} = \xi P_C(\mathbf{a}_i | \mathbf{a}_0) - P_C(\mathbf{a}_j | \mathbf{a}_i)$, $(i, j = 1, 2, \dots, Q)$, $\mathbf{h} \in \mathbb{C}^Q$ with $[\mathbf{h}]_q = M^{-1} \xi - M^{-1} P_C(\mathbf{a}_q | \mathbf{a}_0)$. Please refer to Appendix D for detailed derivation.

In the PBN-BF method, the initial matrix can be chosen as (28). Within the null region of the q -th false target, we define a set of artificial interferences, and the transmit spatial frequency of the l -th artificial interference is formulated as

$$\tilde{f}_T^{lq} = \begin{cases} \tilde{f}_T^q - \frac{1}{2^{\frac{l+1}{2}-1}} \Delta f_T, & l \text{ is odd} \\ \tilde{f}_T^q + \frac{1}{2^{\frac{l}{2}-1}} \Delta f_T, & l \text{ is even} \end{cases}, \quad (34)$$

where \tilde{f}_T^q indicates the transmit spatial frequency that the q -th false target may possible appear.

Adding artificial interferences from Q regions simultaneously in the l -th iteration, the jammer-plus-noise covariance matrix is

$$\mathbf{R}_l = \mathbf{R}_{l-1} + \mathbf{A}_l \mathbf{S}_l \mathbf{A}_l^H, \quad (35)$$

where $\mathbf{A}_l = [\mathbf{a}_{l1}, \mathbf{a}_{l2}, \dots, \mathbf{a}_{lQ}] \in \mathbb{C}^{M \times Q}$ with $\mathbf{a}_{lq} = [1, e^{j2\pi \tilde{f}_T^{lq}}, \dots, e^{j2\pi(M-1)\tilde{f}_T^{lq}}]^T \in \mathbb{C}^M$, and $\mathbf{S}_l = \text{diag}\{\sigma_{l1}^2, \sigma_{l2}^2, \dots, \sigma_{lQ}^2\} \in \mathbb{C}^{Q \times Q}$ denotes the power matrix of the interference during the l -th iteration with $[\mathbf{S}_l]_{q,q} = \sigma_{lq}^2$ being the power of the q -th artificial interference. The inverse matrix of \mathbf{R}_l is

$$\begin{aligned} (\mathbf{R}_l)^{-1} &= (\mathbf{R}_{l-1})^{-1} - (\mathbf{R}_{l-1})^{-1} \\ &\mathbf{A}_l (\mathbf{I} + \mathbf{S}_l \mathbf{A}_l^H (\mathbf{R}_{l-1})^{-1} \mathbf{A}_l)^{-1} \mathbf{S}_l \mathbf{A}_l^H (\mathbf{R}_{l-1})^{-1}. \end{aligned} \quad (36)$$

The weight vector is calculated as

$$\begin{aligned} \mathbf{w}_l &= \Lambda_l (\mathbf{R}_l)^{-1} \mathbf{a}_0 \\ &= \frac{\mathbf{\Gamma}_{l-1} - (\mathbf{R}_{l-1})^{-1} \mathbf{A}_l (\mathbf{I} + \mathbf{S}_l \mathbf{\Upsilon}_l)^{-1} \mathbf{S}_l \mathbf{A}_l^H (\mathbf{R}_{l-1})^{-1} \mathbf{a}_0}{\mathbf{\Gamma}_{l-1}^H \mathbf{a}_0 - \mathbf{\Gamma}_{l-1}^H \mathbf{A}_l (\mathbf{I} + \mathbf{S}_l \mathbf{\Upsilon}_l)^{-1} \mathbf{S}_l \mathbf{A}_l^H (\mathbf{R}_{l-1})^{-1} \mathbf{a}_0}, \end{aligned} \quad (37)$$

where $\mathbf{\Upsilon}_l = \mathbf{A}_l^H (\mathbf{R}_{l-1})^{-1} \mathbf{A}_l \in \mathbb{C}^{Q \times Q}$, $\mathbf{\Gamma}_{l-1} = (\mathbf{R}_{l-1})^{-1} \mathbf{a}_0 \in \mathbb{C}^M$, and the coefficient is:

$$\Lambda_l = \left(\mathbf{a}_0^H (\mathbf{R}_l)^{-1} \mathbf{a}_0 \right)^{-1} \quad (38)$$

For a predefined response of the beampattern, i.e. $P_{\text{opt}l}(\mathbf{a}_q | \mathbf{a}_0) = \mathbf{w}_l^H \mathbf{a}_q = \xi$, the power of the q -th interference signal in the l -th iteration is calculated as

$$\sigma_{lq}^2 = \frac{(\boldsymbol{\eta}_l^H \mathbf{Y}_l^{-1})_q}{(\mathbf{z}_l^H - \boldsymbol{\eta}_l^H \mathbf{Y}_l^{-1} \mathbf{\Upsilon}_l)_q}, \quad (39)$$

where $\mathbf{z}_l \triangleq \mathbf{A}_l^H \mathbf{\Gamma}_{l-1} \in \mathbb{C}^Q$, $\mathbf{Y}_l \triangleq \mathbf{A}_l^H (\mathbf{R}_{l-1})^{-1} (\xi \mathbf{a}_0 \mathbf{1}_Q^T - \mathbf{A}_l) \in \mathbb{C}^{Q \times Q}$ with $[\mathbf{Y}_l]_{:,q} = \mathbf{A}_l^H (\mathbf{R}_{l-1})^{-1} (\xi \mathbf{a}_0 - \mathbf{a}_q)$, and $\boldsymbol{\eta}_l \triangleq \xi \mathbf{1}_Q \mathbf{a}_0^H \mathbf{\Gamma}_{l-1} - \mathbf{A}_l^H \mathbf{\Gamma}_{l-1} \in \mathbb{C}^Q$ with $[\boldsymbol{\eta}_l]_q = \xi \mathbf{a}_0^H \mathbf{\Gamma}_{l-1} - \mathbf{a}_q^H \mathbf{\Gamma}_{l-1}$. Please refer to Appendix E for detailed derivation.

Define a function to collect the positive difference in the l -th iteration as

$$D_l = \frac{1}{Q} \sum_{q=1}^Q \frac{1}{F} \int_{\tilde{f}_T^q - \Delta f_T}^{\tilde{f}_T^q + \Delta f_T} Z(|P_d(f_i)| - \xi) df_i, \quad (40)$$

where $f_i (i = 1, 2, \dots, F)$ indicates the discretized spatial frequency with F being the total numbers of discretized spatial frequencies within Θ_q , the function $Z(x) \triangleq \max\{x, 0\}$, $P_d(f_i)$

Algorithm 1: PBN-BF.

Require: number of false targets Q , ε , prescribed depth ξ ,

$$\mathbf{A} = [\mathbf{a}_1, \mathbf{a}_2, \dots, \mathbf{a}_Q], \beta_{0,j}, \mathbf{a}_0, \sigma_w^2$$

Initialization: $l = 1$

1. Calculate σ_q^2 according to (33) and obtain

$$\mathbf{S}_j = \text{diag}\{\sigma_1^2, \sigma_2^2, \dots, \sigma_Q^2\};$$

2. Obtain $\mathbf{R}_0 = \sigma_w^2 \mathbf{I}_M + \mathbf{A} \mathbf{S}_j \mathbf{A}^H$;

3. Calculate $\Lambda_1 = (\mathbf{a}_0^H (\mathbf{R}_0)^{-1} \mathbf{a}_0)^{-1}$ and

$$\mathbf{w}_1 = \Lambda_1 (\mathbf{R}_0)^{-1} \mathbf{a}_0;$$

4. Calculate D_1 according to (40) using \mathbf{w}_1 ;

while $D_l > \varepsilon$ **do**

5. Select f_{Tq}^l according to (34);

6. Calculate σ_{lq}^2 using (39) and obtain

$$\mathbf{S}_l = \text{diag}\{\sigma_{l1}^2, \sigma_{l2}^2, \dots, \sigma_{lQ}^2\};$$

7. Update $\mathbf{R}_l = \mathbf{R}_{l-1} + \mathbf{A}_l \mathbf{S}_l \mathbf{A}_l^H$;

8. Update $\mathbf{w}_l = \Lambda_l (\mathbf{R}_l)^{-1} \mathbf{a}_0$ using (37);

9. Calculate D_l according to (40) using \mathbf{w}_l ;

10. $l = l + 1$.

end while;

Output: the designed weight vector $\mathbf{w}_d = \mathbf{w}_l$.

TABLE I
SIMULATION PARAMETERS

Parameter	Value	Parameter	Value
M	16	f_0	5.8 GHz
Sample frequency	5 MHz	PRF	20 kHz
Number of pulses	16	Number of range bins	200
Range bin size	30 m	Angle of the target	0°
Range of the target	5 km		

denotes the response of designed beampattern at f_i , and Δf_T represents for the maximum permissible frequency deviation. It is required that $D_l \leq \varepsilon$, and the iterative process continues if $D_l > \varepsilon$. The procedures of the PBN-BF are summarized in Algorithm 1. The main computational complexity lies in calculating the inverse of the jammer-plus-noise covariance matrix for the equivalent transmit beampattern, which is $O(LQM^2)$ with L being the number of total iterations.

With the PBN-BF, a preset equivalent transmit beampattern with broadened notches is obtained. Subsequently, the weight vector is written as

$$\mathbf{w}_{\text{PBN-BF}} = \mathbf{b}(\theta_0) \otimes \mathbf{w}_d. \quad (41)$$

It should be mentioned that with the PBN-BF method, we can still constrain the response of the SOI to be unity, i.e., $\mathbf{w}_{\text{PBN-BF}}^H \mathbf{u}(R_0, \theta_0) = 1$. False targets which deviate from the presumed nulls are located within the broadened notches, where the corresponding responses are constrained to be a minimum predefined value.

IV. SIMULATION RESULTS

In this section, simulations are provided to assess the effectiveness of mainbeam deceptive jammer suppression in UAVs

TABLE II
PARAMETERS OF TARGETS

	True target	False target 1	False target 2	False target 3	False target 4
Angle($^{\circ}$)	0	0	0	0	0
Time delay(ms)	0	0.0267	0.0333	0.1067	0.1400
Delayed pulses	0	1	1	2	3
SNR/JNR (dB)	20	20	25	25	30
Range bin	134	41	68	161	94
Transmit frequency	0	-0.375	-0.375	0.25	-0.125

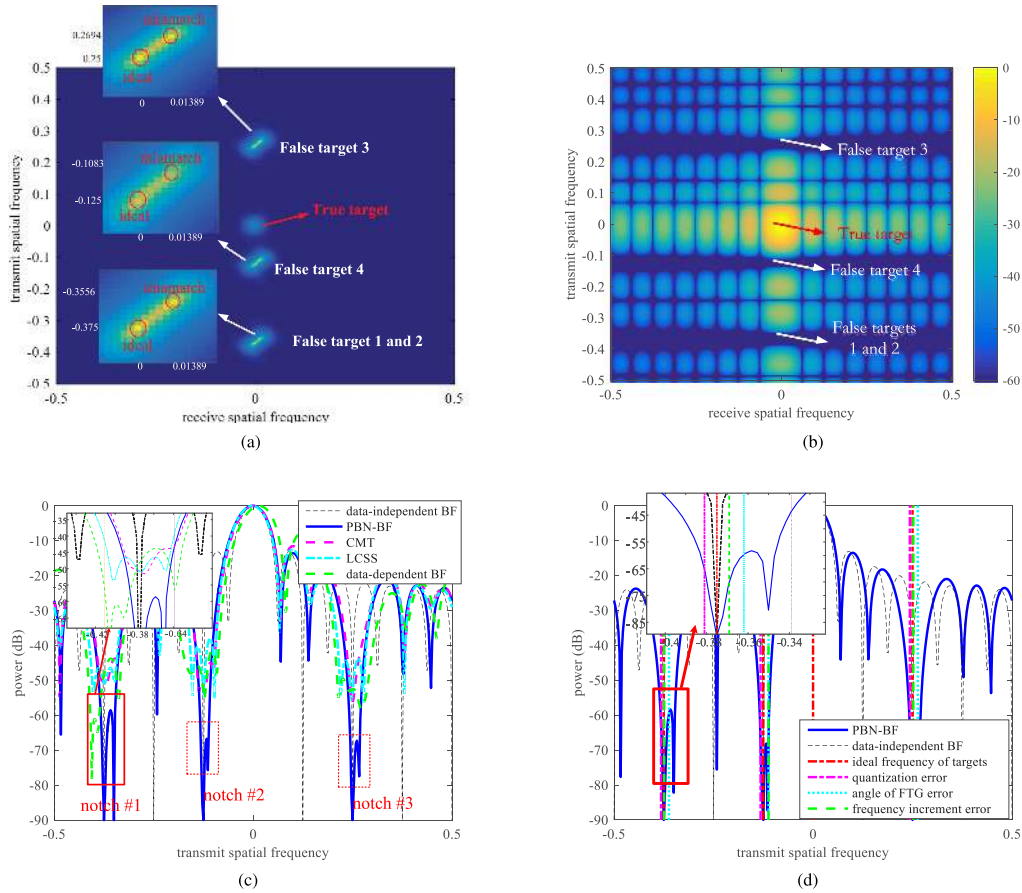


Fig. 5. Results with PBN-BF method. (a) Spectrum distribution in joint transmit-receive domain. (b) Transmit-receive 2-D beampattern. (c) Equivalent transmit beampattern for different methods. (d) Equivalent transmit beampattern with transmit spatial frequency mismatch.

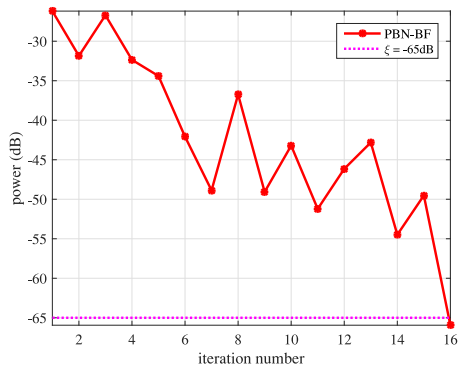


Fig. 6. D_I versus iteration numbers.

using FDA-MIMO scheme. Typically, UAVs have radar operating in the 2.4 GHz and 5.8 GHz band [36], [37]. We assume the carrier frequency at 5.8 GHz, but the proposed method can be ported to other carrier frequencies. Without loss of generality, it is assumed that the elements are half-wavelength spaced. The simulation parameters are listed in Table I. For an operational civil UAV with a maximum weight 20 kg, the maximum detection range is up to 40 km [28], [29]. Hence, the maximum unambiguous range $R_u = 7.5$ km with PRF = 20 kHz is reasonable. Besides, polyphase codes with 100 sub-pulses are considered to be the transmitted waveforms, optimized with the Multi-CAN algorithm [38].

Fig. 4 presents equivalent transmit beampatterns with PBN-BF. Fig. 4(a) shows beampatterns with different Δf_T at the

TABLE III
PERFORMANCE METRICS

	MLSL ratio (dB)	Average depth (dB)	Average SLL (dB)
PBN-BF	13.552	-65.940	-21.078
CMT	11.515	-42.853	-20.043
LCSS	12.577	-46.031	-20.105
Data-dependent BF	7.671	-51.275	-18.207

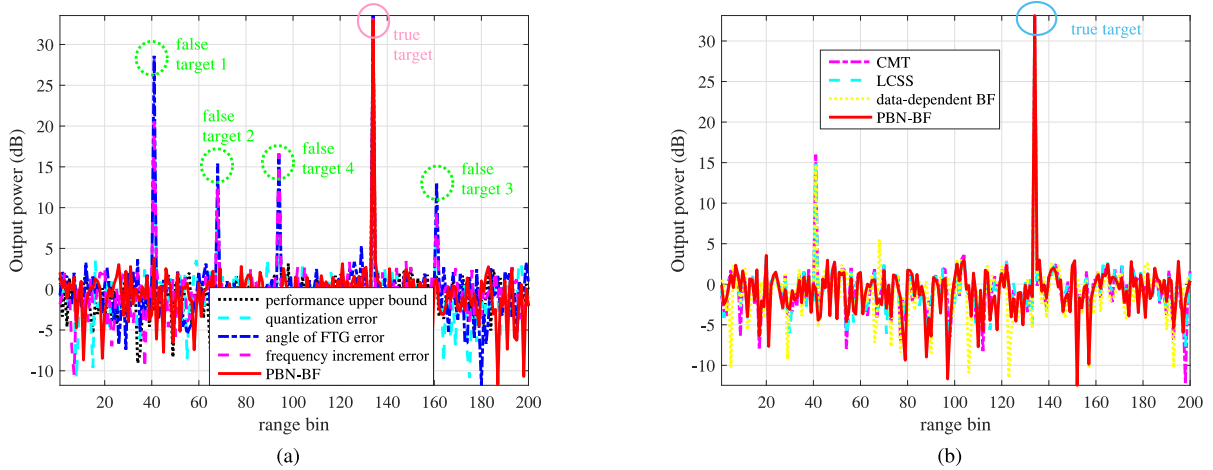


Fig. 7. Output power of matched filtering. (a) Output power with different mismatch factors. (b) Output power with different methods.

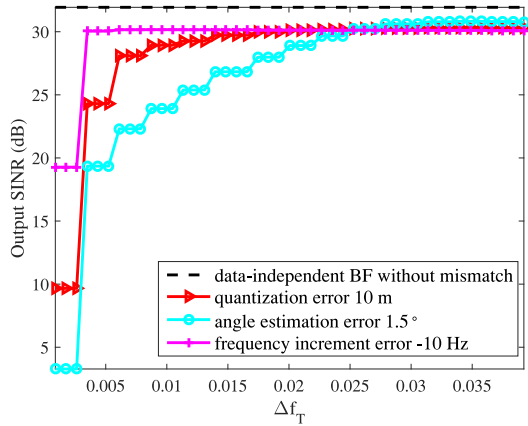


Fig. 8. Output SINR versus f_{Δ} .

6-th null. The width of the null becomes larger and larger with the increase of Δf_T . In practice, the exact knowledge of the mismatch factor is unknown. Hence, in order to consider as many values as possible for the mismatch factor, the notches are broadened about 30% of the mainbeam width, which means a relatively large permissible mismatch region. The beam patterns with different predefined depths are presented in Fig. 4(b). It is shown that a larger depth ξ results in a deeper notch, which enhances the suppression performance. Theoretically, all possible notches should be broadened. In particular, when $u = \frac{1}{M}$, the false target with 1 delayed pulse dwells at the first null point of the beam pattern. In this case, artificial interferences within the mainbeam of the beam pattern will lead to a distortion. To

avoid this problem, a larger u should be selected. Consider a representative example where the first to the fourth null regions are supposed to be broadened because false targets are generated soon to guarantee effective deception. For a false target with a relatively large number of delayed pulses, it should be suppressed to some degrees by the lower sidelobe level. Assume $u = \frac{3}{M}$, Fig. 4(c) presents the designed transmit beam pattern where the first four nulls are broadened with $\Delta f_T = 0.0194$. In contrast, the locations of the first 4 nulls change with $u = \frac{7}{M}$ in Fig. 4(d).

Consider a specific example with four false targets. For simplicity, we assume that there is no range ambiguity for the true target, i.e., $p_s = 0$. Notice that the number of delayed pulses is less than 4, and parameters are given in Table II. It is assumed that the false targets 1, 2 and 4 are settled ahead of the true target with negative range offset, while the false target 3 lags behind the true target with a positive range offset. Moreover, the false targets 1 and 2 have an identical number of delayed pulses. Herein, the frequency increment is 107500 Hz with $z = 5$ and $u = \frac{6}{M}$. Thus, the false target with one delayed pulse dwells at the 6-th null of the beam pattern.

Considering the presence of mismatch, where the angle estimation error is assumed to be 1.5° , and the frequency increment error is -10 Hz. As for the quantization error, for example, the first false target dwells in the 168-th range cell, and its corresponding principle range is 5040 m. However, its actual principle range is 5050 m and the quantization error is $r_{\Delta} = 10$ m. Fig. 5(a) shows the spectrum distributions of true and false targets in the joint transmit-receive domain after range-dependence compensation. Notice that false targets 1 and

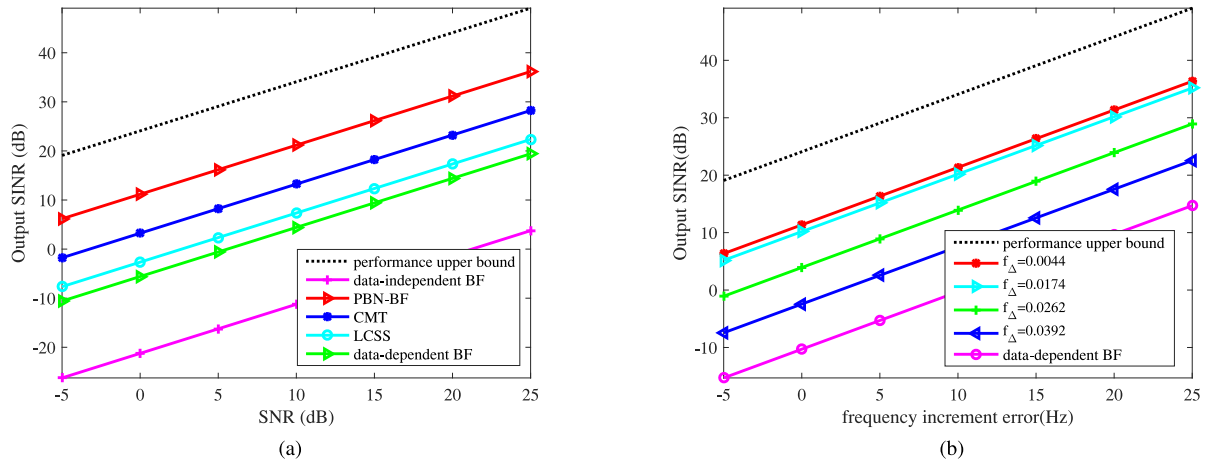


Fig. 9. Output SINR versus input SNR. (a) Output SINR with different methods. (b) Output SINR with different f_{Δ} .

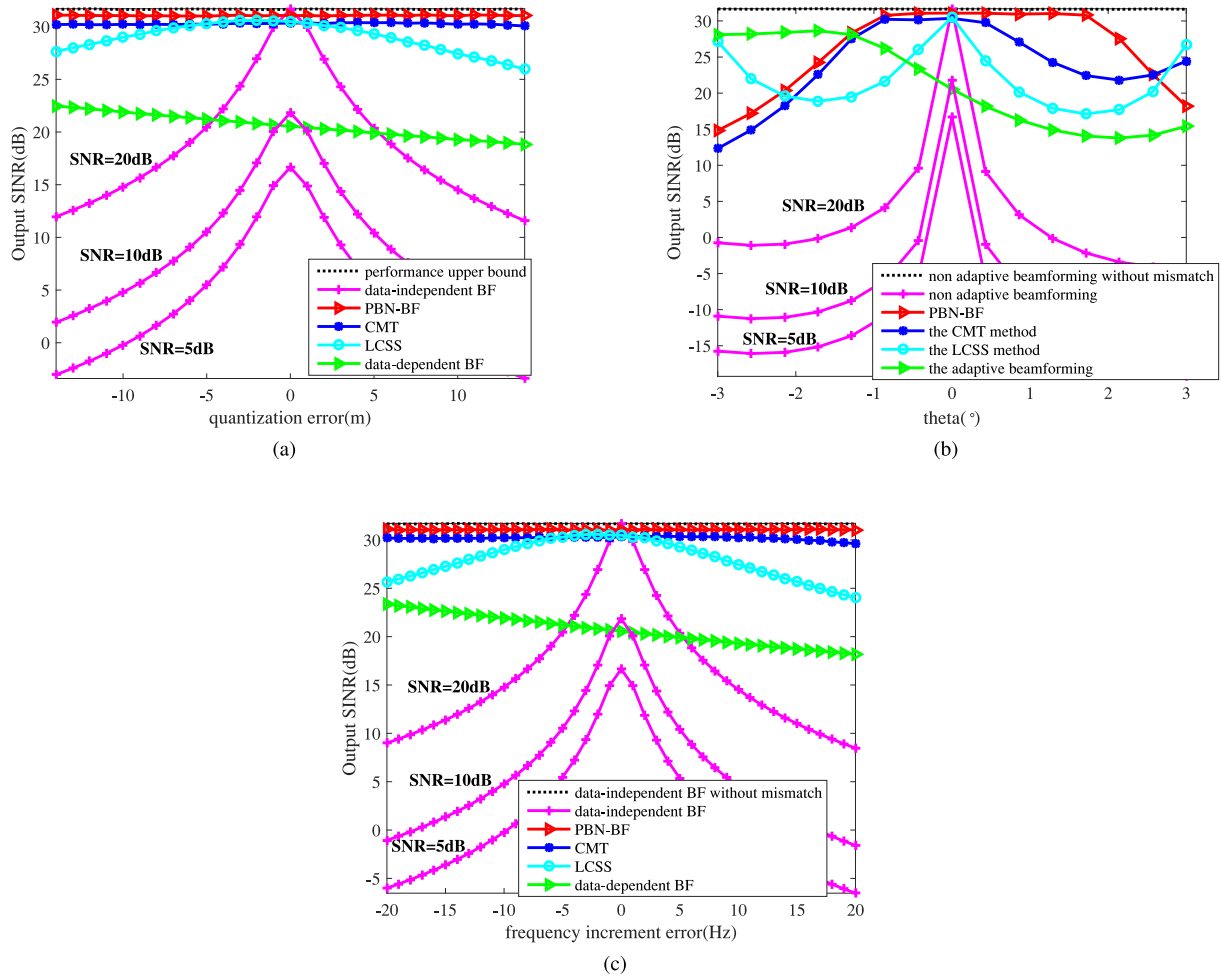


Fig. 10. Output SINR versus different errors. (a) Output SINR with quantization errors. (b) Output SINR with angle estimation errors. (c) Output SINR with frequency increment errors.

2 are located in an identical point because they have identical delayed pulses. It can be seen in the enlarged figures that in the presence of transmit spatial frequency mismatch, there are deviations from their pre-assumed locations. Fig. 5(b) presents the transmit-receive 2-D beampattern with broadened notches and a predefined depth where the maximum permissible deviation of the frequency is assumed as $\Delta f_T = 0.0194$. As depicted in Fig. 5(c), the equivalent transmit beampattern with wide notches and a predefined depth $\xi = -65$ dB is obtained. Compared with the covariance matrix taper (CMT) [33] and linear constraint sector suppressed (LCSS) [34] methods, the PBN-BF has a deeper notch and lower sidelobe level (SLL), which implies the suppression performance is improved. Furthermore, within each null sector, data-dependent BF is performed using 6 interferences with $JNR = 30$ to estimate the jammer-plus-noise covariance matrix [35]. Moreover, four performance metrics, i.e., the maximum main-lobe-to-side-lobe (MLSL) ratio, average sidelobe level, and average depth of the notches are given in Table III. Fig. 5(d) demonstrates the beampattern in the presence of the transmit spatial frequency mismatch. Results show that the frequencies with different errors lead to deviations from their presumed nulls. However, with the PBN-BF, they can still dwell within the notches. Besides, Fig. 6 illustrates the average depths of null steering regions versus iteration numbers, where the D_l drops to -65 dB rapidly after about 16 iterations. The result shows that the proposed method can broaden the nulls with high speed of convergence.

Fig. 7 demonstrates the output power of the matched filter in the presence of transmit spatial frequency mismatch, where the angle estimation error, the frequency increment error, and the quantization error are 1.5° , -10 Hz, and $r_\Delta = 10$ m, respectively. Shown in Fig. 7(a), the output powers of false targets are high when mismatch exists, which in turn generates a high false-alarm ratio. In contrast, with the PBN-BF method, the false targets with both negative and positive range offsets are suppressed, and the maximum power is obtained at the true target. The data-dependent BF in [35] is performed in Fig. 7(b). Compared with the CMT, LCSS, and data-dependent BF methods, the PBN-BF method has no false target residuals at the output of the matched filter in the presence of all errors.

Simulations using Monte Carlo experiments with 200 trials are carried out to evaluate the suppression performance. Fig. 8 plots the output SINR versus f_Δ . It is seen that the larger the width of null sector, the higher the output SINR. Thus, false targets are located within the wide null sectors when transmit spatial frequency mismatch exists, indicating that the robustness of the deceptive jammer suppression is enhanced. The deceptive false targets can be effectively suppressed when $|f_\Delta| \leq \Delta f_T$ is satisfied.

It is demonstrated in Fig. 9(a) that in the presence of transmit spatial frequency mismatch, false targets are effectively suppressed with the PBN-BF method. This leads to a SINR performance improvement compared with the CMT, LCSS and data-dependent BF counterparts. Also, SINR improvement of 30 dB is achieved compared with the conventional data-independent BF. Further simulations are carried out in Fig. 9(b) to show the output SINR versus f_Δ . It is seen that the output

SINR decreases as f_Δ increases. In contrast, for mainbeam deceptive jammer suppression in FDA-MIMO radar using data-dependent beamforming [35], the performance degrades due to insufficient covariance estimation.

The output SINR results versus different errors are plotted in Fig. 10. We observe that the conventional data-independent BF is very sensitive to the arrival angle mismatch, and it is more sensitive when the SNR is lower. Except for the data-independent BF in [35], the methods which can broaden the null steering regions maintain steady output SINR with the varying mismatch. The PBN-BF outperforms the other approaches in terms of output SINR.

V. CONCLUSION

In this paper, we have demonstrated how the mainbeam deceptive jammer is suppressed using the FDA-MIMO scheme for vehicular systems based on data-independent beamforming. It has been realized by setting the false targets at the null points of the equivalent transmit beampattern with an appropriate frequency increment. In practice, deceptive jammers cannot be effectively suppressed when transmit spatial frequency mismatch exists, which occurs due to quantization errors, angle estimation errors and frequency increment errors. The PBN-BF method has been proposed by designing a predefined beampattern with broadened notches where false targets may possibly appear. It has been implemented by adding artificial interferences, and the closed-form expressions of the JNRs have been obtained according to a predefined depth of the null in the beampattern. The jammer-plus-noise covariance matrix is constructed iteratively and the weight vector is obtained. Subsequently, the received signals are processed through a transmit-receive 2-D data-independent BF. Finally, the method has been applied to UAVs, where the mainbeam deceptive jammer has been effectively suppressed. Notice that we focus on jammer suppression for UAV detection, however, our results are also applicable for automotive applications. The results highlight the satisfactory performance of the PBN-BF method in terms of SINR improvement compared with the other BF counterparts.

Future studies could be focused on investigating the jammer suppression performance exploiting different and more complex vehicular systems. Furthermore, the presence and effect of different types of clutter will be considered and modelled.

APPENDIX A DERIVATIONS OF THE RECEIVED SIGNALS AFTER MATCHED FILTERING

Actually, the echo received by each element is a linear combination of all echoes corresponding to M transmit elements. The received signals in (2) are firstly multiplied by $e^{-j2\pi f_0 t}$. Then, the echo is digitally mixed with $e^{-j2\pi(l-1)\Delta f t}$ ($l = 1, \dots, M$), it yields,

$$\bar{y}_n(t, \theta_0) = \alpha_0 e^{j2\pi \frac{d}{\lambda_0} (n-1) \sin(\theta_0)} e^{-j2\pi \Delta f (l-1)t} \sum_{m=1}^M x_m(t - \tau_0) e^{j2\pi \Delta f (m-1)(t-\tau_0)} e^{j2\pi \frac{d}{\lambda_0} (m-1) \sin(\theta_0)}. \quad (42)$$

Then, the received signals pass through a bank of matched filters on each receive channel, where the output of the n -th received signal from the l -th filter, i.e., $h_l(t) = x_l^*(-t)$, is expressed as

$$\begin{aligned} \hat{y}_{n,l}(t, \theta_0) &= \int_{-\infty}^{\infty} \bar{y}_n(\tau, \theta_0) h_l(t - \tau) d\tau \\ &= \alpha_0 e^{j2\pi \frac{d}{\lambda_0} (n-1) \sin(\theta_0)} \sum_{m=1}^M e^{j2\pi \frac{d}{\lambda_0} (m-1) \sin(\theta_0)} \\ &\int_{-\infty}^{\infty} x_m(\tau - \tau_0) x_l^*(\tau - t) e^{j2\pi \Delta f (m-1)(\tau - \tau_0)} e^{-j2\pi \Delta f (l-1)\tau} d\tau \\ &\stackrel{s=\tau-\tau_0}{=} \alpha_0 e^{j2\pi \frac{d}{\lambda_0} (n-1) \sin(\theta_0)} e^{-j2\pi \Delta f (l-1)\tau_0} \sum_{m=1}^M e^{j2\pi \frac{d}{\lambda_0} (m-1) \sin(\theta_0)} \\ &\int_{-\infty}^{\infty} x_m(s) x_l^*(s - (t - \tau_0)) e^{j2\pi \Delta f (m-1)s} e^{-j2\pi \Delta f (l-1)s} ds \\ &= \alpha_0 e^{j2\pi \frac{d}{\lambda_0} (n-1) \sin(\theta_0)} e^{-j2\pi \Delta f (l-1)\tau_0} \\ &\sum_{m=1}^M e^{j2\pi \frac{d}{\lambda_0} (m-1) \sin(\theta_0)} \chi_{l,m}(t - \tau_0, (m-l)\Delta f), \quad (43) \end{aligned}$$

where

$$\begin{aligned} \chi_{l,m}(t - \tau_0, (m-l)\Delta f) &= \int_{-\infty}^{\infty} x_m(s) x_l^*(s - (t - \tau_0)) e^{j2\pi \Delta f (m-l)s} ds \\ &\approx \int_0^{T_p} x_m(s) x_l^*(s) ds = R_{l,m}, \quad (44) \end{aligned}$$

where the approximations rely on the use of pulses whose cross-ambiguities is Doppler tolerant, i.e. the ambiguity function exhibits a flat behavior in a neighborhood of the origin $\chi_{l,m}(0, 0)$. Thus, the signal after matched filtering is expressed as

$$\begin{aligned} \hat{y}_{n,l}(t, \theta_0) &= \alpha_0 e^{j2\pi \frac{d}{\lambda_0} (n-1) \sin(\theta_0)} e^{-j2\pi \Delta f (l-1)\tau_0} \\ &\sum_{m=1}^M R_{l,m} e^{j2\pi \frac{d}{\lambda_0} (m-1) \sin(\theta_0)} \\ &= \alpha_0 e^{j2\pi \frac{d}{\lambda_0} (n-1) \sin(\theta_0)} e^{-j2\pi \Delta f (l-1)\tau_0} e^{j2\pi \frac{d}{\lambda_0} (l-1) \sin(\theta_0)} \tilde{R}_l, \quad (45) \end{aligned}$$

where $\tilde{R}_l = R_{l,l} + e^{-j2\pi \frac{d}{\lambda_0} (l-1) \sin(\theta_0)} \sum_{m=1, m \neq l}^M R_{l,m} e^{j2\pi \frac{d}{\lambda_0} (m-1) \sin(\theta_0)}$.

Subsequently, the received signals from the n -th element can be expressed in a vector form as

$$\begin{aligned} \mathbf{y}_n(t, \theta_0) &= [\hat{y}_{n,1}(t, \theta_0), \hat{y}_{n,2}(t, \theta_0), \dots, \hat{y}_{n,M}(t, \theta_0)]^T \\ &= \alpha_0 e^{j2\pi \frac{d}{\lambda_0} (n-1) \sin(\theta_0)} [\tilde{\mathbf{R}} \odot \mathbf{a}(R_0, \theta_0)], \quad (46) \end{aligned}$$

where $\tilde{\mathbf{R}} = [\tilde{R}_1, \dots, \tilde{R}_M]^T \in \mathbb{C}^M$. Hence, the total received signals of the target are expressed in a $M^2 \times 1$ -dimensional

vector as.

$$\begin{aligned} \mathbf{y}_s &= [\mathbf{y}_1(t, \theta_0), \mathbf{y}_2(t, \theta_0), \dots, \mathbf{y}_M(t, \theta_0)]^T \\ &= \alpha_0 \mathbf{r} \odot [\mathbf{b}(\theta_0) \otimes \mathbf{a}(R_0, \theta_0)], \quad (47) \end{aligned}$$

where $\mathbf{r} = \mathbf{1}_N \otimes \tilde{\mathbf{R}} \in \mathbb{C}^{M^2}$ indicates the output vector of the matched filtering.

APPENDIX B

DERIVATIONS OF THE EQUIVALENT TRANSMIT BEAMPATTERN

The equivalent normalized transmit beampattern is obtained with summation of components of the transmit steering vector after range compensation, which is

$$\begin{aligned} P(f_T) &= \mathbf{w}_T^H \tilde{\mathbf{a}}(f_T) = \frac{1}{M} \cdot \sum_{m=1}^M e^{j2\pi (m-1)f_T} \\ &= \frac{1}{M} \cdot \frac{1 - e^{j2\pi M f_T}}{1 - e^{j2\pi f_T}} \\ &= \frac{1}{M} \cdot \frac{e^{j\pi M f_T} (e^{-j\pi M f_T} - e^{j\pi M f_T})}{e^{j\pi f_T} (e^{-j\pi f_T} - e^{j\pi f_T})} \\ &= \frac{1}{M} \cdot e^{j\pi (M-1)f_T} \frac{\sin(\pi M f_T)}{\sin(\pi f_T)}, \quad (48) \end{aligned}$$

where $\mathbf{w}_T = \frac{1}{M} [1, \dots, 1]^T \in \mathbb{R}^M$, $\tilde{\mathbf{a}}(f_T) = [1, e^{j2\pi f_T}, \dots, e^{j2\pi (M-1)f_T}]^T \in \mathbb{C}^M$ denotes the transmit steering vector after range compensation, and $f_T = \frac{d}{\lambda_0} \sin(\theta_0)$.

APPENDIX C

DERIVATIONS WITH SUCCESSIVE ARTIFICIAL INTERFERENCE CONSTRUCTION

Using the matrix inversion lemma, the inverse matrix is

$$\mathbf{R}_1^{-1} = \frac{1}{\sigma_w^2} \left[\mathbf{I}_M - \frac{\sigma_1^2}{\sigma_w^2 + M\sigma_1^2} \mathbf{a}_1 \mathbf{a}_1^H \right]. \quad (49)$$

Subsequently, the weight vector is

$$\mathbf{w}_1 = \Lambda_1 \mathbf{R}_1^{-1} \mathbf{a}_0 = \frac{\Lambda_1 M}{\sigma_w^2} \left[\frac{\mathbf{a}_0}{M} - \beta_{01} \frac{\sigma_1^2}{\sigma_w^2 + M\sigma_1^2} \mathbf{a}_1 \right], \quad (50)$$

where $\beta_{01} = \frac{\mathbf{a}_0^H \mathbf{a}_1}{M}$ and $\Lambda_1 = \left\{ \frac{1}{\sigma_w^2} M \left[1 - \frac{M\sigma_1^2}{\sigma_w^2 + M\sigma_1^2} |\beta_{01}|^2 \right] \right\}^{-1}$. Subsequently, the beampattern is calculated as

$$\begin{aligned} P_{\text{opt1}}(\mathbf{a} | \mathbf{a}_0) &= \mathbf{w}_1^H \mathbf{a} \\ &= \frac{\Lambda_1 M}{\sigma_w^2} \left[P_C(\mathbf{a} | \mathbf{a}_0) - \frac{M\rho_1 \beta_{01}}{1 + M\rho_1} \cdot P_C(\mathbf{a} | \mathbf{a}_1) \right], \quad (51) \end{aligned}$$

where $\rho_1 \triangleq \frac{\sigma_1^2}{\sigma_w^2}$, $P_C(\mathbf{a} | \mathbf{a}_i)$ denotes the beampattern with the mainbeam at \mathbf{a}_i .

As $P_{\text{opt1}}(\mathbf{a}_1 | \mathbf{a}_0) = \xi$ is desired, the power of the first interference is calculated as

$$\sigma_1^2 = \rho_1 \sigma_w^2 = \frac{\sigma_w^2}{M} \cdot \frac{\beta_{01} - \xi}{\xi (1 - |\beta_{01}|^2)}. \quad (52)$$

Then, after imposing the second interference, the jammer-plus-noise covariance matrix is updated as

$$\mathbf{R}_2 = \mathbf{R}_1 + \sigma_2^2 \mathbf{a}_2 \mathbf{a}_2^H. \quad (53)$$

The weight vector is updated as

$$\begin{aligned} \mathbf{w}_2 &= \Lambda_2 \mathbf{R}_2^{-1} \mathbf{a}_0 \\ &= \Lambda_2 \left[(\mathbf{R}_1)^{-1} \mathbf{a}_0 - \frac{\sigma_2^2 (\mathbf{R}_1)^{-1} \mathbf{a}_2 \mathbf{a}_2^H (\mathbf{R}_1)^{-1} \mathbf{a}_0}{1 + \sigma_2^2 \mathbf{a}_2^H (\mathbf{R}_1)^{-1} \mathbf{a}_2} \right], \end{aligned} \quad (54)$$

where $\Lambda_2 = \{\mathbf{a}_0^H [(\mathbf{R}_1)^{-1} - \frac{\sigma_2^2 (\mathbf{R}_1)^{-1} \mathbf{a}_2 \mathbf{a}_2^H (\mathbf{R}_1)^{-1}}{1 + \sigma_2^2 \mathbf{a}_2^H (\mathbf{R}_1)^{-1} \mathbf{a}_2}] \mathbf{a}_0\}^{-1}$.

According to $P_{\text{opt}2}(\mathbf{a}_2 | \mathbf{a}_0) = \xi$, the power of the second interference is calculated as

$$\sigma_2^2 = \frac{\mathbf{a}_0^H (\mathbf{R}_1)^{-1} (\mathbf{a}_2 - \xi \mathbf{a}_0)}{\xi \mathbf{a}_0^H (\mathbf{R}_1)^{-1} [\mathbf{a}_0 \mathbf{a}_2^H (\mathbf{R}_1)^{-1} \mathbf{a}_2 - \mathbf{a}_2 \mathbf{a}_2^H (\mathbf{R}_1)^{-1} \mathbf{a}_0]}. \quad (55)$$

Subsequently, the power of the q -th interference is calculated using mathematical induction as

$$\sigma_q^2 = \frac{\mathbf{a}_0^H (\mathbf{R}_{q-1})^{-1} (\mathbf{a}_q - \xi \mathbf{a}_0)}{\xi \mathbf{a}_0^H (\mathbf{R}_{q-1})^{-1} [\mathbf{a}_0 \mathbf{a}_q^H (\mathbf{R}_{q-1})^{-1} \mathbf{a}_q - \mathbf{a}_q \mathbf{a}_q^H (\mathbf{R}_{q-1})^{-1} \mathbf{a}_0]}. \quad (56)$$

When adding the Q -th interference, the final jammer-plus-noise covariance matrix is updated as

$$\begin{aligned} \mathbf{R}_Q &= \mathbf{R}_{Q-1} + \sigma_Q^2 \mathbf{a}_Q \mathbf{a}_Q^H \\ &= \mathbf{R}_{Q-2} + \sigma_{Q-1}^2 \mathbf{a}_{Q-1} \mathbf{a}_{Q-1}^H + \sigma_Q^2 \mathbf{a}_Q \mathbf{a}_Q^H \\ &= \mathbf{R}_0 + \sum_{q=1}^Q \sigma_q^2 \mathbf{a}_q \mathbf{a}_q^H \end{aligned} \quad (57)$$

APPENDIX D

DERIVATIONS WITH CONCURRENT ARTIFICIAL INTERFERENCE CONSTRUCTION

The value of the transmit beampattern at \mathbf{a}_q with a predefined depth ξ is calculated as

$$\begin{aligned} P_{\text{opt}}(\mathbf{a}_q | \mathbf{a}_0) &= \Lambda \mathbf{w}^H \mathbf{a}_q = \xi \\ &= \frac{M\Lambda}{\sigma_w^2} \left[P_C(\mathbf{a}_q | \mathbf{a}_0) - M\beta_{0J}^H (\mathbf{I}_Q + \Sigma_J \mathbf{A}^H \mathbf{A})^{-1} \right. \\ &\quad \left. \Sigma_J \mathbf{P}_C(\mathbf{a}_q | \mathbf{a}_J) \right] \\ &= \frac{P_C(\mathbf{a}_q | \mathbf{a}_0) - M\beta_{0J}^H (\mathbf{I}_Q + \Sigma_J \mathbf{A}^H \mathbf{A})^{-1} \Sigma_J \mathbf{P}_C(\mathbf{a}_q | \mathbf{a}_J)}{1 - \beta_{0J}^H (\mathbf{I}_Q + \Sigma_J \mathbf{A}^H \mathbf{A})^{-1} \Sigma_J M\beta_{0J}}, \end{aligned} \quad (58)$$

where $\mathbf{P}_C(\mathbf{a}_q | \mathbf{a}_J) \triangleq \frac{\mathbf{A}^H \mathbf{a}_q}{M} \in \mathbb{C}^Q$ denotes the beampattern response vector for Q regions, $P_C(\mathbf{a}_q | \mathbf{a}_i) = \frac{\mathbf{a}_i^H \mathbf{a}_q}{M}$, ($i = 1, 2, \dots, Q$) is the response of the conventional beampattern which is pointed at the steering vector \mathbf{a}_i and evaluated with \mathbf{a}_q . Define $\mathbf{P} \in \mathbb{C}^{Q \times Q}$ with $[\mathbf{P}]_{i,j} = \xi P_C(\mathbf{a}_i | \mathbf{a}_0) - P_C(\mathbf{a}_j | \mathbf{a}_i)$, ($j = 1, 2, \dots, Q$) and $\mathbf{h} \in \mathbb{C}^Q$ with $[\mathbf{h}]_q = M^{-1} \xi - M^{-1} P_C(\mathbf{a}_q | \mathbf{a}_0)$. Thus, we have a set

of Q equations to be determined, and the problem is expressed as

$$\beta_{0J}^H (\mathbf{I}_Q + \Sigma_J \mathbf{A}^H \mathbf{A})^{-1} \Sigma_J \mathbf{P} = \mathbf{h}^H. \quad (59)$$

Notice that since Σ_J , \mathbf{A} , and \mathbf{P} are both $Q \times Q$ full-rank matrices, the matrix $(\mathbf{I}_Q + \Sigma_J \mathbf{A}^H \mathbf{A})$ is a nonsingular matrix. Firstly both sides of the equation are multiplied by \mathbf{P}^{-1} and Σ_J^{-1} sequentially. The equation is processed by the following steps:

$$\begin{aligned} \beta_{0J}^H \left[\mathbf{I}_Q - \Sigma_J (\Sigma_J + (\mathbf{A}^H \mathbf{A})^{-1})^{-1} \right] &= \mathbf{h}^H \mathbf{P}^{-1} \Sigma_J^{-1} \\ (\beta_{0J}^H - \mathbf{h}^H \mathbf{P}^{-1} \Sigma_J^{-1}) (\Sigma_J + (\mathbf{A}^H \mathbf{A})^{-1}) &= \beta_{0J}^H \Sigma_J \\ \beta_{0J}^H - \mathbf{h}^H \mathbf{P}^{-1} \mathbf{A}^H \mathbf{A} &= \mathbf{h}^H \mathbf{P}^{-1} \Sigma_J^{-1} \\ (\beta_{0J}^H - \mathbf{h}^H \mathbf{P}^{-1} \mathbf{A}^H \mathbf{A}) \Sigma_J &= \mathbf{h}^H \mathbf{P}^{-1}. \end{aligned} \quad (60)$$

Notice that $\mathbf{h}^H \mathbf{P}^{-1}$ and $\beta_{0J}^H - \mathbf{h}^H \mathbf{P}^{-1} \mathbf{A}^H \mathbf{A}$ are both $1 \times Q$ vectors. As Σ_J is a diagonal matrix, the JNR of the q -th interference is expressed as

$$[\Sigma_J]_{q,q} = \rho_q = \frac{[\mathbf{h}^H \mathbf{P}^{-1}]_q}{[\beta_{0J}^H - \mathbf{h}^H \mathbf{P}^{-1} \mathbf{A}^H \mathbf{A}]_q}. \quad (61)$$

It follows the power of the q -th interference as

$$\sigma_q^2 = \rho_q \sigma_w^2 = \frac{[\mathbf{h}^H \mathbf{P}^{-1}]_q}{[\beta_{0J}^H - \mathbf{h}^H \mathbf{P}^{-1} \mathbf{A}^H \mathbf{A}]_q} \sigma_w^2. \quad (62)$$

APPENDIX E

SOLUTIONS TO POWERS OF INTERFERENCES WITH PBN-BF

The beampattern evaluated at \mathbf{a}_q is calculated as

$$\begin{aligned} P_{\text{opt}l}(\mathbf{a}_q | \mathbf{a}_0) &= \mathbf{w}_l^H \mathbf{a}_q \\ &= \frac{\Gamma_{l-1}^H \mathbf{a}_q - \Gamma_{l-1}^H \mathbf{A}_l \mathbf{S}_l (\mathbf{I} + \mathbf{S}_l \Upsilon_l)^{-1} \mathbf{A}_l^H (\mathbf{R}^{(l-1)})^{-1} \mathbf{a}_q}{\Gamma_{l-1}^H \mathbf{a}_0 - \Gamma_{l-1}^H \mathbf{A}_l (\mathbf{I} + \mathbf{S}_l \Upsilon_l)^{-1} \mathbf{S}_l \mathbf{A}_l^H (\mathbf{R}^{(l-1)})^{-1} \mathbf{a}_0} \\ &= \xi. \end{aligned} \quad (63)$$

For Q false targets, it is further expressed as

$$\mathbf{z}_l^H (\mathbf{I}_Q + \mathbf{S}_l \Upsilon_l)^{-1} \mathbf{S}_l \mathbf{Y} = \boldsymbol{\eta}_l^H, \quad (64)$$

where $\mathbf{z}_l \triangleq \mathbf{A}_l^H \Gamma_{l-1} \in \mathbb{C}^Q$, $\mathbf{Y}_l \triangleq \mathbf{A}_l^H (\mathbf{R}_{l-1})^{-1} (\xi \mathbf{a}_0 \mathbf{1}_Q^T - \mathbf{A}_l) \in \mathbb{C}^{Q \times Q}$ with $[\mathbf{Y}_l]_{:,q} = \mathbf{A}_l^H (\mathbf{R}_{l-1})^{-1} (\xi \mathbf{a}_0 - \mathbf{a}_q)$, and $\boldsymbol{\eta}_l \triangleq \xi \mathbf{1}_Q \mathbf{a}_0^H \Gamma_{l-1} - \mathbf{A}_l^H \Gamma_{l-1} \in \mathbb{C}^Q$ with $[\boldsymbol{\eta}_l]_q = \xi \mathbf{a}_0^H \Gamma_{l-1} - \mathbf{a}_q^H \Gamma_{l-1}$.

Since \mathbf{S}_l , Υ_l , and \mathbf{Y} are all $Q \times Q$ full-rank matrices, thus $(\mathbf{I}_Q + \mathbf{S}_l \Upsilon_l)^{-1} \mathbf{S}_l \mathbf{Y}_l$ is a nonsingular matrix, thus, after multiplied by $[(\mathbf{I}_Q + \mathbf{S}_l \Upsilon_l)^{-1} \mathbf{S}_l \mathbf{Y}_l]^{-1}$ to both sides of the equation simultaneously, the equation is finally expressed as

$$\mathbf{z}_l^H - \boldsymbol{\eta}_l^H \mathbf{Y}_l^{-1} \Upsilon_l = \boldsymbol{\eta}_l^H \mathbf{Y}_l^{-1} \mathbf{S}_l^{-1}. \quad (65)$$

Then, the power of the q -th artificial interference in the l -th iteration is calculated as

$$\sigma_{lq}^2 = \frac{(\boldsymbol{\eta}_l^H \mathbf{Y}_l^{-1})_q}{(\mathbf{z}_l^H - \boldsymbol{\eta}_l^H \mathbf{Y}_l^{-1} \Upsilon_l)_q}. \quad (66)$$

Thus, the power matrix in the l -th iteration is given by

$$\mathbf{S}_l = \text{diag} \{ \sigma_{l1}^2, \sigma_{l2}^2, \dots, \sigma_{lQ}^2 \}. \quad (67)$$

ACKNOWLEDGMENT

The authors would like to thank the editor and the anonymous reviewers for their time and constructive comments to improve the quality of the manuscript.

REFERENCES

- [1] X. Yu, G. Cui, J. Yang, and L. Kong, "MIMO radar transmit-receive design for moving target detection in signal-dependent clutter," *IEEE Trans. Veh. Technol.*, vol. 69, no. 1, pp. 522–536, Jan. 2020.
- [2] F. Jin and S. Cao, "Automotive radar interference mitigation using adaptive noise canceller," *IEEE Trans. Veh. Technol.*, vol. 68, no. 4, pp. 3747–3754, Apr. 2019.
- [3] L. Li, K. Ota, and M. Dong, "Humanlike driving: Empirical decision-making system for autonomous vehicles," *IEEE Trans. Veh. Technol.*, vol. 67, no. 8, pp. 6814–6823, Aug. 2018.
- [4] L. Xiao, C. Xie, M. Min, and W. Zhuang, "User-centric view of unmanned aerial vehicle transmission against smart attacks," *IEEE Trans. Veh. Technol.*, vol. 67, no. 4, pp. 3420–3430, Apr. 2018.
- [5] S. Alland, W. Stark, M. Ali, and M. Hegde, "Interference in automotive radar systems: Characteristics, mitigation techniques, and current and future research," *IEEE Signal Process. Mag.*, vol. 36, no. 5, pp. 45–59, Sep. 2019.
- [6] J. Hu, Y. Wu, R. Chen, F. Shu, and J. Wang, "Optimal detection of UAV's transmission with beam sweeping in covert wireless networks," *IEEE Trans. Veh. Technol.*, vol. 69, no. 1, pp. 1080–1085, Jan. 2020.
- [7] Y. Huang, L. Zhang, J. Li, Z. Chen, and X. Yang, "Reweighted tensor factorization method for SAR narrowband and wideband interference mitigation using smoothing multiview tensor model," *IEEE Trans. Geosci. and Remote Sens.*, vol. 58, no. 5, pp. 3298–3313, May 2020.
- [8] J. Bechter, F. Roos, M. Rahman, and C. Waldschmidt, "Automotive radar interference mitigation using a sparse sampling approach," in *Proc. Eur. Radar Conf.*, Nuremberg, 2017, pp. 90–93.
- [9] M. Soumekh, "SAR-ECCM using phase-perturbed LFM chirp signals and DRFM repeat jammer penalization," *IEEE Trans. Aerosp. Electron. Syst.*, vol. 42, no. 1, pp. 191–205, Jan. 2006.
- [10] G. Hakobyan and B. Yang, "High-performance automotive radar: A review of signal processing algorithms and modulation schemes," *IEEE Signal Process. Mag.*, vol. 36, no. 5, pp. 32–44, Sep. 2019.
- [11] S. Sruthy, A.-H. Akram, J. E. Robin, S. Kandeepan, P. Udaya, "Interference mitigation in automotive radars using pseudo-random cyclic orthogonal sequences," *Sensors*, vol. 19, pp. 1–19, 2019.
- [12] J. Akhtar, "Orthogonal block coded ECCM schemes against repeat radar jammers," *IEEE Trans. Aerosp. Electron. Syst.*, vol. 45, no. 3, pp. 1218–1226, Jul. 2009.
- [13] J. Akhtar, K. Olsen, "Frequency agility radar with overlapping pulses and sparse reconstruction," in *Proc. IEEE Radar Conf.*, Oklahoma, OK, USA, Apr. 2018, pp. 61–66.
- [14] Y. Quan, Y. Wu, Y. Li, G. Sun, M. Xing, "Range-Doppler reconstruction for frequency agile and PRF-jittering radar," *IET Radar Sonar Navigat.*, vol. 12, no. 3, pp. 348–352, Mar. 2018.
- [15] P. Antonik, M. C. Wicks, H. D. Griffiths, C. J. Baker, "Frequency diverse array radars," in *Proc. IEEE Conf. Radar*, Verona, NY, USA, Apr. 2006, pp. 215–217.
- [16] A. Basit, W. Khan, S. Khan, and I. M. Qureshi, "Development of frequency diverse array radar technology: A review," *IET Radar, Sonar Navigat.*, vol. 12, no. 2, pp. 165–175.
- [17] W.-Q. Wang, "Overview of frequency diverse array in radar and navigation applications," *IET Radar, Sonar Navigat.*, vol. 10, no. 6, pp. 1001–1012, Jul. 2016.
- [18] P. Gong, W.-Q. Wang, F. Li, H.-C. So, "Sparsity-aware transmit beamspace design for FDA-MIMO radar," *Signal Process.*, vol. 144, pp. 99–103, Mar. 2018.
- [19] Y. Ma, P. Wei, and H. Zhang, "General focusing beamformer for FDA: Mathematical model and resolution analysis," *IEEE Trans. Antennas Propag.*, vol. 67, no. 5, pp. 3089–3100, May 2019.
- [20] A. Basit, W.-Q. Wang, S. Y. Nusenu, and S. Zhang, "Range-angle-dependent beampattern synthesis with null depth control for joint radar communication," *IEEE Antennas Wireless Propag. Lett.*, vol. 18, no. 9, pp. 1741–1745, Sep. 2019.
- [21] Y. Liu, H. Ruan, L. Wang, A. Nehorai, "The random frequency diverse array: A new antenna structure for uncoupled direction-range indication in active sensing," *IEEE J. Sel. Topics Signal Process.*, vol. 11, no. 2, pp. 295–308, Mar. 2017.
- [22] C. Wen, M. Tao, J. Peng, J. Wu, and T. Wang, "Clutter suppression for airborne FDA-MIMO radar using multi-waveform adaptive processing and auxiliary channel STAP," *Signal Process.*, vol. 154, pp. 280–293, Jan. 2019.
- [23] C. Wang, J. Xu, G. Liao, X. Xu, and Y. Zhang, "A range ambiguity resolution approach for high-resolution and wide-swath SAR imaging using frequency diverse array," *IEEE J. Sel. Topics Signal Process.*, vol. 11, no. 2, pp. 336–346, Mar. 2017.
- [24] S. Y. Nusenu, and W.-Q. Wang, "Range-dependent spatial modulation using frequency diverse array for OFDM wireless communications," *IEEE Trans. Veh. Technol.*, vol. 67, no. 11, pp. 10886–10895, Nov. 2018.
- [25] J. Xu, G. Liao, S. Zhu, H. C. So, "Deceptive jamming suppression with frequency diverse MIMO radar," *Signal Process.*, vol. 113, pp. 9–17, Jan. 2015.
- [26] L. Lan, G. Liao, J. Xu, Y. Zhang, and F. Fioranelli, "Suppression approach to main-beam deceptive jamming in FDA-MIMO radar using nonhomogeneous sample detection," *IEEE Access*, vol. 6, no. 1, pp. 34582–34597, Jun. 2018.
- [27] J. Xu, J. Kang, G. Liao, and H. C. So, "Mainlobe deceptive jammer suppression with FDA-MIMO radar," in *Proc. SAM*, Sheffield, UK, Jul. 2018, pp. 504–508.
- [28] A. C. Watts, V. G. Ambrosia, and E. A. Hinkley, "Unmanned aircraft systems in remote sensing and scientific research: Classification and considerations of use," *Remote Sens.*, vol. 4, no. 6, pp. 1671–1692, 2012.
- [29] G. Singhal, B. Bansod, and L. Mathew, "Unmanned aerial vehicle classification, applications and challenges: A review," *Preprints*, 2018, doi: 10.20944/preprints201811.0601.v1.
- [30] M. G. Erdemli, "General use of UAS in EW environment—EW concepts and tactics for single or multiple UAS over the net-centric battlefield," Master's thesis, Nav. Postgrad. School, Monterey, CA, USA, Sep. 2009.
- [31] J. Xu, G. Liao, S. Zhu, L. Huang, and H. C. So, "Joint range and angle estimation using MIMO radar with frequency diverse array," *IEEE Trans. Signal Process.*, vol. 63, no. 13, pp. 3396–3410, Jul. 2015.
- [32] C. A. Olen and R. T. Compton, "A numerical pattern synthesis algorithm for arrays," *IEEE Trans. Antennas Propag.*, vol. 38, no. 10, pp. 1666–1676, Oct. 1990.
- [33] J. G. Guerci, "Theory and application of covariance matrix tapers for robust adaptive beamforming," *IEEE Trans. Signal Process.*, vol. 47, no. 4, pp. 977–985, Apr. 1999.
- [34] A. Amar and M. A. Doron, "A linearly constrained minimum variance beamformer with a pre-specified suppression level over a pre-defined broad null sector," *Signal Process.*, vol. 109, pp. 165–171, 2015.
- [35] L. Lan, G. Liao, J. Xu, A method to suppress the main-beam deceptive jamming in FDA-MIMO radar with random polyphase codes, in *Proc. SAM*, Sheffield, U.K., Jul. 2018, pp. 509–513.
- [36] B.-H. Louisa, *Unmanned Aerial Vehicles (Drones): An Introduction*, House of Commons Library, U.K., 2012.
- [37] S. Y. Jun, A. Shastri, B. Sanz-Izquierdo, D. Bird, and A. McClelland, "Investigation of antennas integrated into disposable unmanned aerial vehicles," *IEEE Trans. Veh. Technol.*, vol. 68, no. 1, pp. 604–612, Jan. 2019.
- [38] H. He, P. Stoica, and J. Li, "Designing unimodular sequence sets with good correlations—including an application to MIMO radar," *IEEE Trans. Signal Process.*, vol. 57, no. 11, pp. 4391–4405, Jun. 2009.



Lan Lan (Member, IEEE) was born in Xi'an, China in 1993. She received the B.S. degree in electronic engineering, and the Ph.D. degree in signal and information processing, both from Xidian University, Xi'an, China, in 2015 and 2020, respectively. She has been a Visiting Ph.D. Student with the University of Naples "Federico II," Italy, from 2019 to 2020. She is currently a Tenure-Track Associated Professor with the National Laboratory of Radar Signal Processing, Xidian University, from August 2020.

Her research interests include frequency diverse array radar systems, MIMO radar signal processing, target detection and ECCM. She was a recipient of the Excellent Paper Award at the CIE 2016 International Conference on Radar.



Hong Kong.

His research interests include radar system modeling, multi-sensor array signal processing, space-time adaptive processing, multiple-input multiple-output radar, and waveform diverse array radar.

Jingwei Xu (Member, IEEE) was born in Shandong, China. He received the B.S. degree in electronic engineering, and the Ph.D. degree in signal and information processing, both from Xidian University, China, in 2010 and 2015, respectively. He is currently an Associated Professor with the School of Electronic Engineering, Xidian University. From 2015 to 2017, he was a Lecturer with the National Lab of Radar Signal Processing in Xidian University. From 2017 to 2019, he was a Postdoctoral Fellow under “Hong Kong Scholar Program” at the City University of



Francesco Fioranelli (Senior Member, IEEE) received the Ph.D. degree from Durham University, U.K., in 2014. He is currently Assistant Professor with TU Delft in the Netherlands, and was an Assistant Professor with the University of Glasgow, from 2016 to 2019 and Research Associate with University College London, from 2014 to 2016.

His research interests include the development of radar systems and techniques for automatic target classification in applications including human signatures analysis in healthcare and security, drones and UAVs detection and classification, automotive radar, wind farm signatures and sea clutter.



Guisheng Liao (Senior Member, IEEE) was born in Guilin, Guangxi, China in 1963. He received the B.S. degree from Guangxi University, Guangxi, China, in 1985, and the M.S. and Ph.D. degrees from Xidian University, Xi'an, China, in 1990, and 1992, respectively.

He is currently a Yangtze River Scholars Distinguished Professor with the National Laboratory of Radar Signal Processing and serves as Dean of the School of Electronic Engineering, in Xidian University. Since 2009, He has been the evaluation expert

for the international cooperation project of Ministry of Science and Technology in China. Since 2007, he has been the lead of Yangtze River Scholars Innovative Team and devoted in advanced techniques in signal and information processing. Since 2006, he has served as the panelists for the medium and long term development plan in high-resolution and remote sensing systems. From 1999 to 2000, He has been a Senior Visiting Scholar in the Chinese University of Hong Kong, Hong Kong.

His research interests include array signal processing, space-time adaptive processing, radarwaveform design, and airborne/space surveillance andwarning radar systems.



Hing Cheung So (Fellow, IEEE) was born in Hong Kong. He received the B.Eng. degree from the City University of Hong Kong and the Ph.D. degree from The Chinese University of Hong Kong, both in electronic engineering, in 1990 and 1995, respectively. From 1990 to 1991, he was an Electronic Engineer with the Research and Development Division, Everex Systems Engineering Ltd., Hong Kong. During 1995 to 1996, he was a Postdoctoral Fellow with The Chinese University of Hong Kong. From 1996 to 1999, he was a Research Assistant Professor with the

Department of Electronic Engineering, City University of Hong Kong, where he is currently a Professor. His research interests include detection and estimation, fast and adaptive algorithms, multidimensional harmonic retrieval, robust signal processing, source localization, and sparse approximation.

He has been on the editorial boards of *IEEE Signal Processing Magazine* (2014 to 2017), *IEEE TRANSACTIONS ON SIGNAL PROCESSING*, in 2010 to 2014, *Signal Processing* (2010), and *Digital Signal Processing* (2011). He was also Lead Guest Editor for *IEEE JOURNAL OF SELECTED TOPICS IN SIGNAL PROCESSING*, Special Issue on “Advances in Time/Frequency Modulated Array Signal Processing,” in 2017. In addition, he was an Elected Member in Signal Processing Theory and Methods Technical Committee (2011 to 2016) of the IEEE Signal Processing Society where he was Chair in the awards subcommittee (2015 to 2016).



Yuhong Zhang (Senior Member, IEEE) received the B.S., M.S., and Ph.D. degrees from Xidian University, Xi'an, China, in 1982, 1984, and 1988, respectively, all in electrical engineering. He is currently a Professor with Electronic Engineering School, Xidian University. From 1998 to 2014, he was a Senior Scientist at Stiefvater Consultants, and Research Associates for Defense Conversion Inc., Rome, NY, USA, and worked on-site at the Air Force Research Laboratory in Rome, NY, from 1998 to 2010. From 1994 to 1998, he was at Syracuse University, Syracuse, NY, as a

Visiting Associate Professor. From 1988 to 1993, he was with the Institute of Electronic Engineering at Xidian University, and served as an Associate Professor and the Deputy Director of the Institute.

His current research interests include array signal processing, remote sensing, signal modeling and simulation, SAR imaging, and waveform diversity.